Investigation of microstructure, hardness and residual stresses of wire and arc additive manufactured 6061 aluminium alloy

Gautier Doumenc, Laurent Couturier, Bruno Courant, Pascal Paillard, Alexandre Benoit, Eric Gautron, Baptiste Girault, Thilo Pirling, Sandra Cabeza, David Gloaguen

Investigation of microstructure, hardness and residual stresses of wire and arc additive manufactured 6061 aluminium alloy

Gautier Doumenc[1,2,3,] Laurent Couturier[2], Bruno Courant[3], Pascal Paillard[2], Alexandre Benoit[1], Eric Gautron[2], B. Girault[3], Thilo Pirling[4], Sandra Cabeza[4], David Gloaguen[3]

1: IRT Jules Verne, Technocampus Composite, Chemin du Chaffault, 44340 Bouguenais, France

2: Nantes Université, CNRS, Institut des Matériaux de Nantes Jean Rouxel, IMN, F-44000 Nantes, France

3: Nantes Université, Ecole Centrale Nantes, CNRS, Institut de Recherche en Génie Civil et Mécanique , GeM, F-44600 Saint-Nazaire, France.

4: Institut Laue-Langevin, 71 Avenue des Martyrs, 38000 Grenoble, France

Corresponding authors:

gautier.doumenc@hotmail.com

Keywords
Wire and Arc Additive Manufacturing, 6XXX, Microstructure, Residual stress

ABSTRACT

Wire and Arc Additive Manufacturing Cold Metal Transfer® enable the defect-free soldering of poorly weldable alloys, such as AA6061. Thin-walls have been successfully built with two deposition strategies that is either a back and forth movement of the torch (alternate deposition vectors) or a repeating movement along one direction (unidirectional deposition vectors). The obtained macro- and micro-structures are highly dependent on the WAAM process parameters and the deposition strategy. Both deposition strategies produce stacked structures consisting of successive alternating layers of columnar and equiaxial grains. The AA6061 alloy contains iron-rich intermetallic compounds and β-phase. The precipitates of the latter have been melted during the WAAM deposition process leading to an even higher hardness as compared to the commercial T6 material. At the nanoscale, Transmission Electron Microscopy analyses reveal β' phase, β'' phase and small dispersoids at T6 state, as well as a multitude of phases (L, Q') in the studied material. It shows the coexistence of β''- and β'- phases. The conventional T6 treatment applied to the WAAM material resulted in a slight over-ageing of this material. Neutron diffraction has been used for residual stress measurements showing tensile stresses (up to 130 MPa) in the built parts and compressive stresses (up to - 80 MPa) in the substrate. Despite a difference between the generated microstructure (grain shape orientation and subsequent crystallographic texture) by the two building strategies, no significant variation has been observed on their mechanical properties.

1. INTRODUCTION

Additive Manufacturing (AM) shows a great expansion due to the technological stake it represents. It enables repairing worn-out parts (building up), lightening structures, manufacturing parts with complex geometries and displays a large industrial adaptability [1–4]. Wire and Arc Additive Manufacturing (WAAM) is a DED (Direct Energy Deposition) process that represents an interesting solution for large scale structures requiring low cost fast manufacturing. It combines an electric arc as a heat source and a wire filler as a feedstock. Compared to other AM processes, WAAM techniques provide a high material deposition rate, a relatively low cost and the ability to manufacture large metre-scale components of medium geometric complexity [4,6]. However, a final operation of machining is usually required in order to obtain precise geometrical features from the produced near-net-shape part. Most of the time, a material surplus is deposited to foresee this machining operation [7,8]. As for the other AM processes, a preliminary study focused on microstructure and mechanical properties in relation with process parameters is also mandatory to overcome uncontrolled microstructural evolution, large residual stresses, cracks and geometrical distortions [4].

Thanks to their properties such as high specific strength combined with natural corrosion resistance, age hardening aluminium alloys such as Aluminium Alloy 6061 (AA6061) are widely used in many structural applications. Hence, AA6061 stands as a good candidate when using a high deposition rate process such as WAAM for structural applications. Its mechanical properties mainly stem from the nanometric β''-phase precipitation, an intermetallic compound rich in Mg and Si (Mg_5Si_6) [9]. β''-phase is metastable and generally precipitates in a well-controlled manner during dedicated heat treatment but is only one of the many intermetallic phases that can be encountered in this type of alloy. However, the actual microstructure of the WAAM-produced part remains unknown due to the complex out of equilibrium thermal history.

6XXX alloy series are also well-known for their poor weldability [10,11]. The Al/Mg ratio set around 0.8 makes it highly susceptible to hot cracking and, as all aluminium alloys, it has a natural trend to generate porosities because of the high solubility of hydrogen in the liquid aluminium that drops down to almost zero in the solid aluminium [12,13]. It is common to use filler wire metals with other compositions (4XXX or 5XXX alloys) to avoid harmful hot cracking [14,15]. The same drawbacks naturally appear in WAAM. In the literature, a substantial work on AM of aluminium alloys with PBF-Laser technique shows that all types of aluminium alloys are printable using this particular process [16]. In contrast, recent studies on WAAM show that only specific 2XXX [17–25], 4XXX [26–30] and 5XXX [20,22,27,28,30–36] series can be successfully deposited. Thus, an upstream development is absolutely required to obtain WAAM-built parts using 6XXX and 7XXX series of aluminium alloys [37,38]. Recent investigations on process parameters enabling the welding of the 6061 aluminium alloy were carried out by Benoit *et al.* [39] and Kumar *et al.* [40]. But to date, even though Al-Mg-Si-Cu alloys are widely used for structural applications, there is no detailed studies regarding the ability to use AA6061 for Wire and Arc Additive Manufacturing [4]. The recent development of a Metal Inert Gas (MIG) transfer mode based on a low-energy short-circuit, called Cold Metal Transfer (CMT®), made possible the use of 6XXX age hardening aluminium alloys for welding [35,39,41–43]. However, those studies have been limited to simple welding. To our knowledge, no study on AM with AA6061 has been achieved until now.

Additively built parts using WAAM undergo a complex thermal history: high heating and cooling rates leading to strong out of equilibrium state, subjected to successive solidification, thermal expansion, high-temperature gradients, phase transformations, ageing of precipitated minor phases. This affects both the microstructure and the residual stress distribution. The optimization of MIG-CMT to widen the use of WAAM in miscellaneous industries necessarily involves the in-depth knowledge of the mechanical and metallurgical states of the produced parts to ensure the best in-service performances. Therefore, the present work aims to link microstructural features, hardness and residual stresses in additively manufactured AA6061. The purpose is to investigate the process parameters enabling the built of a defect-free material using WAAM as well as the understanding of the relationship between the particular WAAM built microstructure and the resulting mechanical properties. Two deposition strategies (namely alternate (zigzag) or unidirectional vectors) have also been investigated in order to control the microstructures as shown by Dinda with DED-Laser process [43] and by Yehorov *et al.* with WAAM process [24]. In addition, after a heat treatment, a higher hardness is obtained for WAAM parts as compared to conventional forged products. The microstructure of AA6061 parts produced by WAAM has been evaluated in order to assess and understand these hardening phenomena.

2. EXPERIMENTAL DETAILS

2.1. Filler wire

As mentioned above, AA6061 is considered to be non-weldable, hence there is no commercially available filler wire. AA6061-filler wire has been drawn on demand for the study from a single 6061 aluminium alloy billet. The composition, measured using (Electron Dispersive Spectroscopy) EDS, is presented and discussed in section 3.1.

2.2. Deposition process

AA6061 thin-wall samples have been deposited on AA1050 plates with a size of 2×30×250 mm^3 by MIG-CMT process developed by Fronius® [44]. CMT is a specific MIG transfer mode based on dip transfer deposition, characterised by a well-controlled material drop deposition during the short circuit of the wire electrode to the substrate, decreasing the energy required for the material deposition. Hence, it is called cold metal transfer due to the low energy used compared with the other transfer modes available in MIG welding [45]. Compared with other welding techniques, MIG-CMT seems a suitable candidate for WAAM of age hardening aluminium alloys due to the low applied heat input. Temperature has been measured with three thermocouples positioned within the baseplate to follow the temperature evolution during WAAM.

A Cartesian robot with step-by-step motors equipped with a welding device Fronius® TransPuls Synergic 3200 CMT compose the experimental set-up (Fig. 1(a)). A water-cooling system regulates the bottom of the clamped AA1050 baseplate at 20°C, as described in Figure 1(b). The welding torch working distance is set at 15 mm.

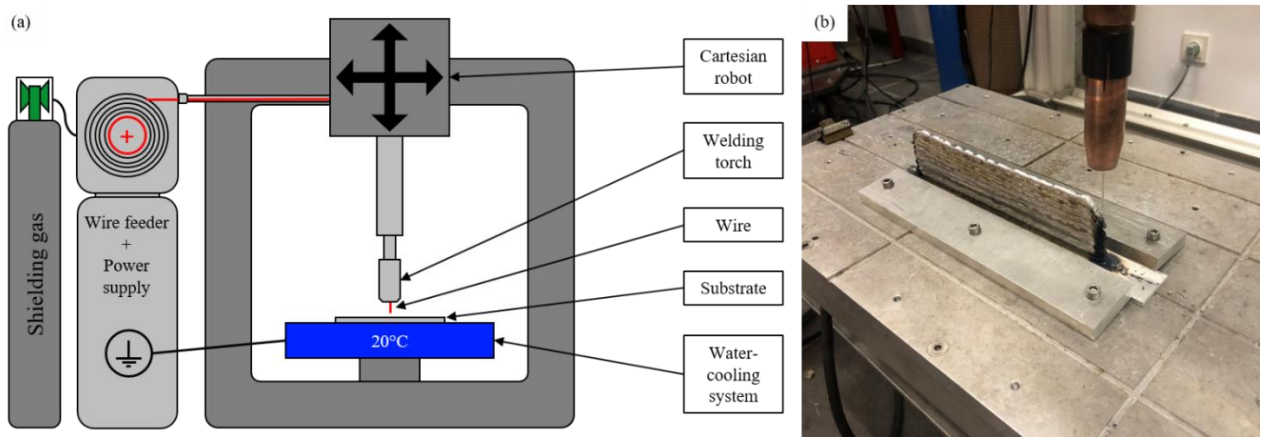

Figure 1 : (a) Schematic experimental set up for deposition. (b) details of base plate clamping and cooling devices.

WAAM is a complex multi-parameter process. Deposition parameters have been chosen by trial and error starting with the standard parameters pre-recorded within the welding station – welding synergies – and appropriate adjustments. Only parts obtained with suitable parameters to ensure a good material health are considered in this study. Torch speed has been kept constant at 40 $cm.s^{-1}$. A parameter optimization protocol based on Mezrag *et al.* [46] and Ortega *et al.* [26] works ensuring the optimal stability of the WAAM process (based on the respect of the CMT cycle monitored by a high-speed camera and electrical measurements) allowed us to find the optimal Wire Feed Speeds (WFS) at 4.3 $m.min^{-1}$. A commercial mixture composed of 80% argon and 20% helium has been used as a shielding gas [2,10]. A higher wire feed speed (5 $m.min^{-1}$) has been used for the preliminary adhesion layer deposition to prevent necking and delamination from the base plate.

Additionally, two different deposition strategies (namely alternate or unidirectional vectors) have been studied using the same set of process parameters (set-up, heat input level, travel speed, WFS) to understand how these strategies influence the microstructural features and the development of residual stresses within the built part. An adaptive cooling time has been taken in order to reach 20°C in the baseplate before each layer deposition. This time never exceeded 40 s

2.3. Heat treatments

6XXX aluminium alloys series are precipitation hardened. The temperature and the duration of ageing enabling an optimal strengthening are approximately 170°C and 8 hours, respectively. This particular heat treatment is known as T6. The microstructure formed during the additive manufacturing process within the produced part is unknown and should present marked heterogeneities. The as-deposited state is therefore studied. This as-deposited microstructure is not stable over time, so we are also interested in characterising the stable microstructure obtained after natural ageing.

Different metallurgical states have been characterised:

- As-Deposited (denoted AD): material has been kept at -80°C after printing to prevent natural ageing,
- Naturally Aged (NA/T4): material has been kept at room temperature during at least two weeks after deposition (no solutionizing in-between),
- Forced Maturation (M): material has undergone a maturation at 90°C during 2 h to evaluate its hardness stability,
- Peak aged (T6): material has been solutionized at 530°C during 1 h, then water quenched and finally aged at 175°C during 8 h.

2.4. Specimen preparation and equipment

X-ray radiography has been conducted with a GE TITAN E 160 at 160 kV and 40 mA with a pause time of 15 s. The X-ray shot has been carried out with a single-film using the plane to plane technique. Specimen surfaces for porosity investigation and hardness tests were prepared under a standard procedure of surface dressing and pre-polishing with series of 180-grit, 500-grit, 800-grit, 1200-grit, and 2000-grit silicon carbide (SiC) papers.

The Vickers microhardness tests were carried out with a STRUERS DuraScan under a load of 0.1 kgf and a holding time of 10 s. Hardness maps were measured using a square grid with a 2 mm step.

Samples for metallographic observations and EBSD specimens have undergone the same preparation, completed by a polishing step with a 3 µm and 1 µm diamond solution. Finally, they were polished using a colloidal neutral silica suspension (0.04 µm) for 8h to reach a strain-free mirror finish. Metallographic samples have been subsequently etched with Barker's electrolytic reagent (5 mL HBF_4, 200 mL H_2O) during 2 minutes at 30 V. Microstructures have been examined under polarised light using a ZEISS AXIO Imager M2 optical microscope.

Fine microstructure features and intermetallic phases have been characterised employing a ZEISS Merlin Field Emission Gun Scanning Electron Microscope (FEG-SEM) equipped with an energy dispersive spectrometer Oxford X-Max. The latter instrument has been used to determine the chemical compositions of the wire and the WAAM deposited material. Electron Back Scatter Diffraction (EBSD) analyses were performed using the ZEISS Merlin FEG-SEM together with an EBSD Nordlys 2 HKL (Oxford Instruments) probe. An accelerating voltage of 20 kV and a beam current of 1 nA were used for the acquisitions. The results have been collected and processed with the Channel 5 software.

Nanometric scale phases have been studied using Transmission Electron Microscopy (TEM). Samples have been grinded down to 75 µm thick foils. Then, 3 mm-diameter disks were punched out of these foils and prepared for TEM observations by electropolishing with a twin-jet polisher TENUPOL-5 at -25 °C and under 15 V with an etchant composed of 30% commercially pure (around 70%) nitric acid and 70% methanol in volume. A Thermo Fisher Scientific S-TEM Themis Z G3 has been used for fine metallurgical studies. TEM micrographs and electron diffraction patterns were acquired with a CMOS One View camera (Gatan).

2.5. Residual stress measurements

To understand the stress development, Neutron Diffraction (ND) experiments have been carried out on SALSA (Strain Analyser for Large and Small scale engineering Applications) beamline at Laue Langevin Institute (ILL). More details of this instrument are available in the work of Pirling *et al.* [49]. The gauge has a volume of $2\times2\times2$ mm^3 and the {311} diffraction peak of aluminium ($2\theta = 88.5°$ with a wavelength of 1.62 Å) is considered for the measurements. As presented in Figure 2 (a), the stress field investigation has been achieved along a column in the middle of the thin-wall sample. Measurement points ensure a reliable determination of the stress gradient regarding to the microstructure length scale (Figure 2 (d)). Asymmetrically distributed gauge positions over the height of the wall have been probed. An additional point has been taken at the centre of the baseplate to understand its role in the residual stress equilibrium. Lattice strain have been measured along the three orthogonal directions, matching the sample coordinates system at each measurement point, in order to provide an assessment of the three normal

strain components ε_{xx} ε_{yy}, and ε_{zz}. The experimental set-up for the three measurement directions is described in Figure 2.

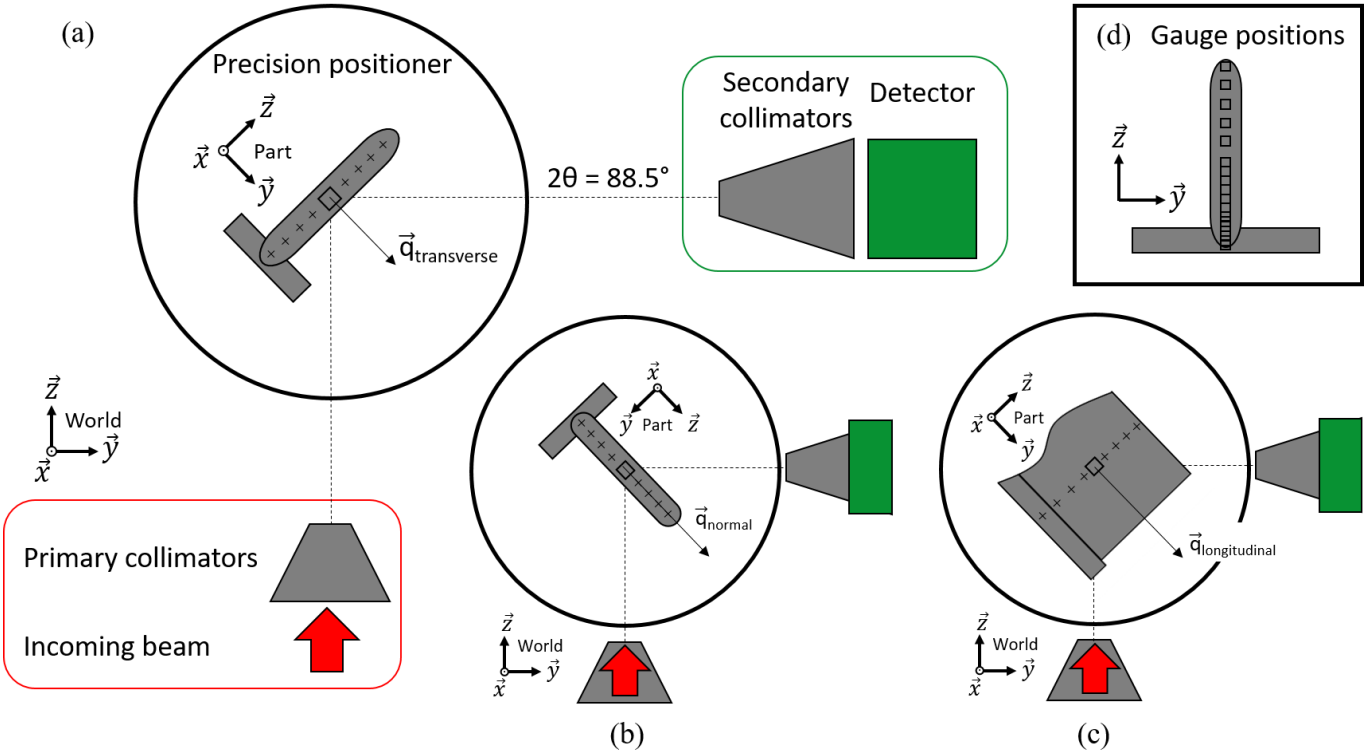

Figure 2 : Schematic illustration of the set-up for neutron measurements (a) for transverse direction (Y) ; (b) for normal direction (Z) ; (c) for longitudinal direction (X) ; (d) gauge positions.

3. RESULTS & DISCUSSION

3.1. Part geometries

Defect-free AA6061 thin-walls have been successfully built with two different deposition strategies (alternate or unidirectional deposition vectors). The welding parameters have been chosen in order to ensure the CMT cycle stability, so that no spatter was produced during material deposition. Geometries of the deposited walls have been measured using a Mitutoyo 500 digital calliper. The aim was to produce walls of 150×5×50 mm^3 dimensions once machined. To achieve this, as reported in the introduction, a 1 mm additional thickness is added to the targeted 5 mm to allow for the finishing machining step [7,8]. Figure 3 illustrates the as-deposited wall geometries achieved for both strategies prior to the final machining operation.

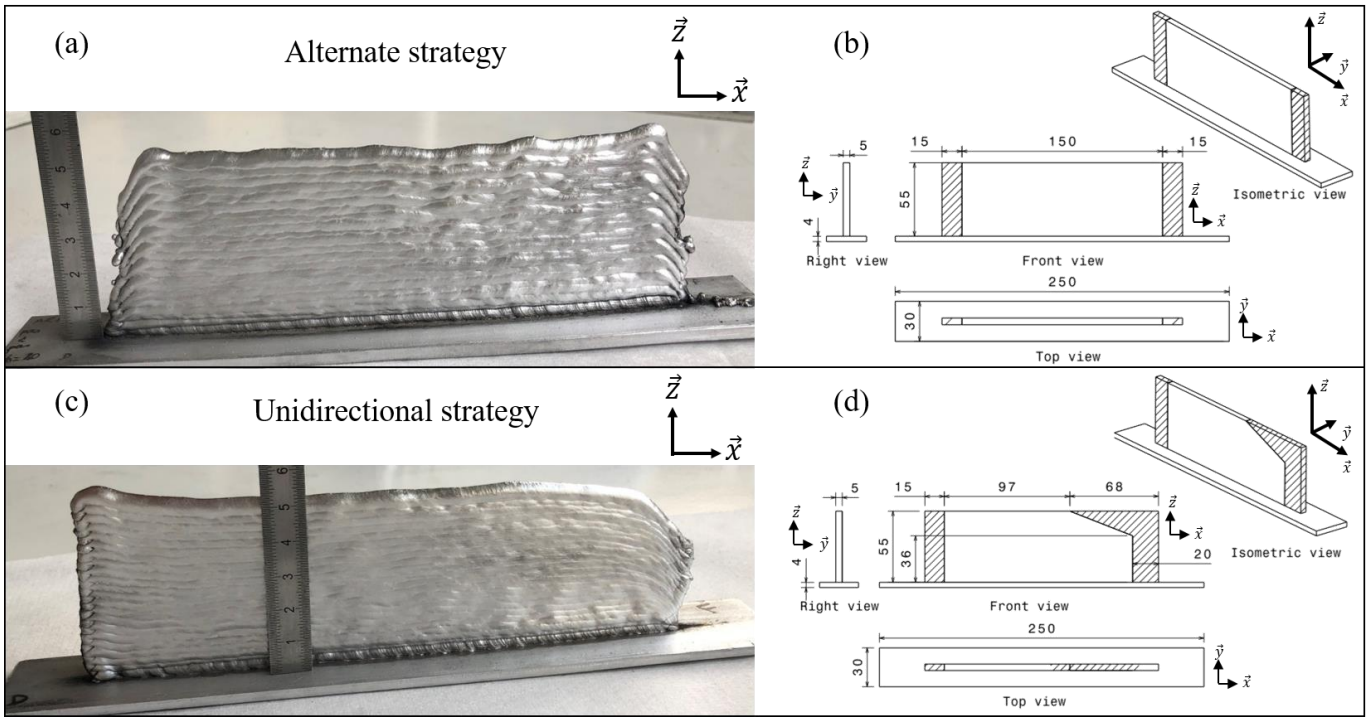

Figure 3: (a) geometry of the as deposited thin-wall for the alternate strategy ; (b) final part geometry for the alternate strategy ; (c) geometry of the as deposited thin-wall for the unidirectional strategy ; (d) final part geometry for the unidirectional strategy.

Figure 3 presents two of the built samples: one for the alternate strategy (a and b) and one for the unidirectional strategy (c and d). One can observe from the pictures of the walls (i.e. Figure 3.a and Figure 3.c) that the shape of the built walls is different. Indeed, the slight excess of material at the start of the welding bead and the slight lack of it at the end, added over the successive bead depositions for the unidirectional strategy, lead to an asymmetric shape with a large excess of material on the starting side and a large lack of it on the ending side of the welding beads. This effect has already been reported in the literature by Zhang *et al.* [50]. As proposed by the authors, we can observe on Figure 3.a that the use of an alternate strategy enables to compensate these excesses and lacks of material over two welding beads in opposite directions, leading to a final wall with a correct symmetric shape, as desired. It may be noted here that the choice of a building strategy strongly modifies the grain structure within the building. This aspect, shown in section 3.5, especially using EBSD, will be discussed later in section 4 since it may have a strong influence on the mechanical strength of the resulting part and has to be taken into consideration. The effective wall thickness is 5 mm and the surface waviness is 0.8 mm [8]. There is no preferable strategy regarding the surface waviness and the effective wall thickness. Therefore, we aimed for a 6 mm as-built mean thickness.

3.2. Chemical composition

The global composition of the deposit has been measured using EDS and compared to the composition measured in the filler wire. The results presented in Table 1 show that both compositions are close.

Table 1: Chemical composition of the AA6061wire filler and for the AA6061-part built by WAAM

Elements	Mg	Si	Cr	Fe	Ti	Zn	Mn	Cu	Al	Total
AA6061 Wire Filler wt%	0.91	0.99	0.13	0.29	0.01	0.16	0.07	0.20	97.24	100.00
AA6061 as-deposited wt%	0.87	1.05	0.09	0.29	0.01	0.10	0.05	0.13	97.41	100.00
AA6061 Nominal Composition wt% [51]	0.81 - 1.20	0.40 - 0.80	0.04 - 0.35	max 0.70	max 0.15	max 0.25	max 0.15	0.15 - 0.40	bal.	100.00

Preferential evaporation from the weld pool of some elements, presenting a high vapour pressure such as Zn, Mn and Mg, can be significant regardless of the temperature [52,53]. Even if several elements could be vaporized, sample composition prepared by WAMM remains within the nominal composition range given by the standard for AA6061, except for Si (excess) and Cu (depletion) contents [51]. However, the Si content was already out of range in the filler material and only slightly varies. Cu content, although remaining in the composition range for the wire filler, was in the low range and its slight variation may be attributed to evaporation that causes a slight depletion with respect to the standard.

3.3. Material health

3.3.1 X-Ray inspection

The visual inspections on machined samples showing neither cracks nor obvious porosities, X-Ray inspection has been carried out to detect any defects that would not be visible to the naked eye (within the material or on the surface but too small to be detected). Walls have been machined on both sides to avoid artefacts due to the raw surface condition. As we can see in Figure 4, walls built with both strategies are almost free from defects. Only a limited number of porosities can be found in the very first layer (close to the baseplate), which is the adhesion layer. This adhesion layer has been built with parameters reducing the CMT stability in order to enhance the wettability and to counteract the very high thermal extraction from the baseplate. Porosities are also present near the top surface in the last layer, being the only welding bead not reheated and partially melted by a coming up welding pass. Hence, the largest porosities are found in that last deposited layer which is more likely to be machined for most industrial applications to get the net shape of the additively manufactured part.

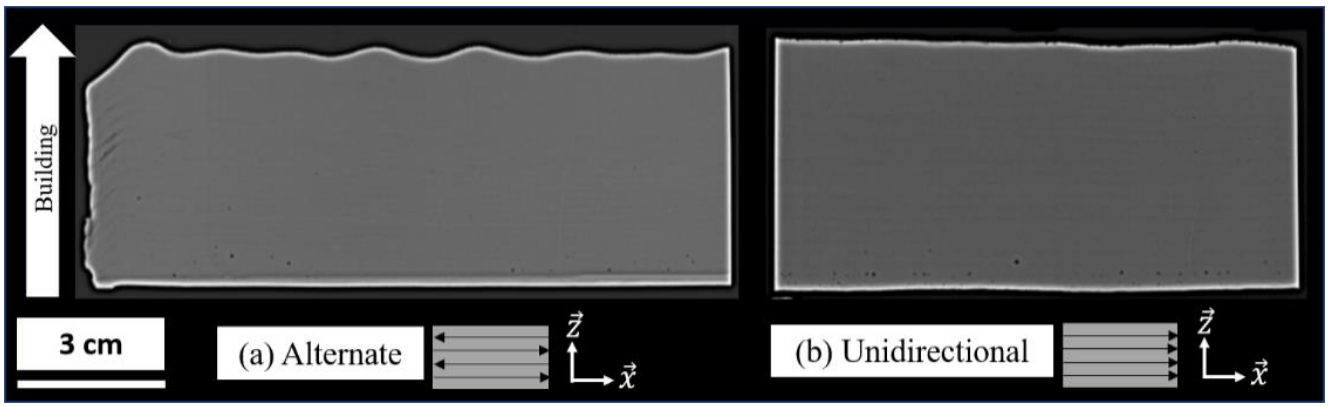

Figure 4 : X-Ray radiographs of the deposited walls (a) alternate strategy (b) unidirectional strategy.

3.3.2 Optical microscope investigations

Porosity measurement has been performed by image analysis with the Trainable Weka Segmentation of Fiji software [54]. Evaluation has been carried out on macrographs along the longitudinal direction (XZ plane) and extracted in the centre region of the specimen to evaluate the efficiency of the chosen parameters. Based on OM observations, the porosity fraction appears very low (< 0.2%) and the maximum measured pore size is 170 µm. One reason stands in the careful cleaning and degreasing of the baseplate prior to the first layer deposition. This step is very important in order to avoid pollutants like grease to be cracked within the electric arc producing hydrogen that can be solutionized in the liquid aluminium and then leading to the apparition of porosities upon solidification when the hydrogen solubility drops down to almost zero. An additional cause for the low fraction of porosities is the use of a He-rich shielding gas making possible to raise the arc plasma temperature, maintaining a less viscous melt pool and thus a better hydrogen degassing from the liquid pool. Porosities can however still be found in the first layer which is an adhesion layer made with a higher wire feed speed (5 $m.s^{-1}$) and in the last layer due to incomplete hydrogen degassing.

3.4. Hardness

As can be seen in Figure 6, the hardness is relatively constant throughout the thickness (i.e. along the Y direction) of the samples regardless of the building strategy.

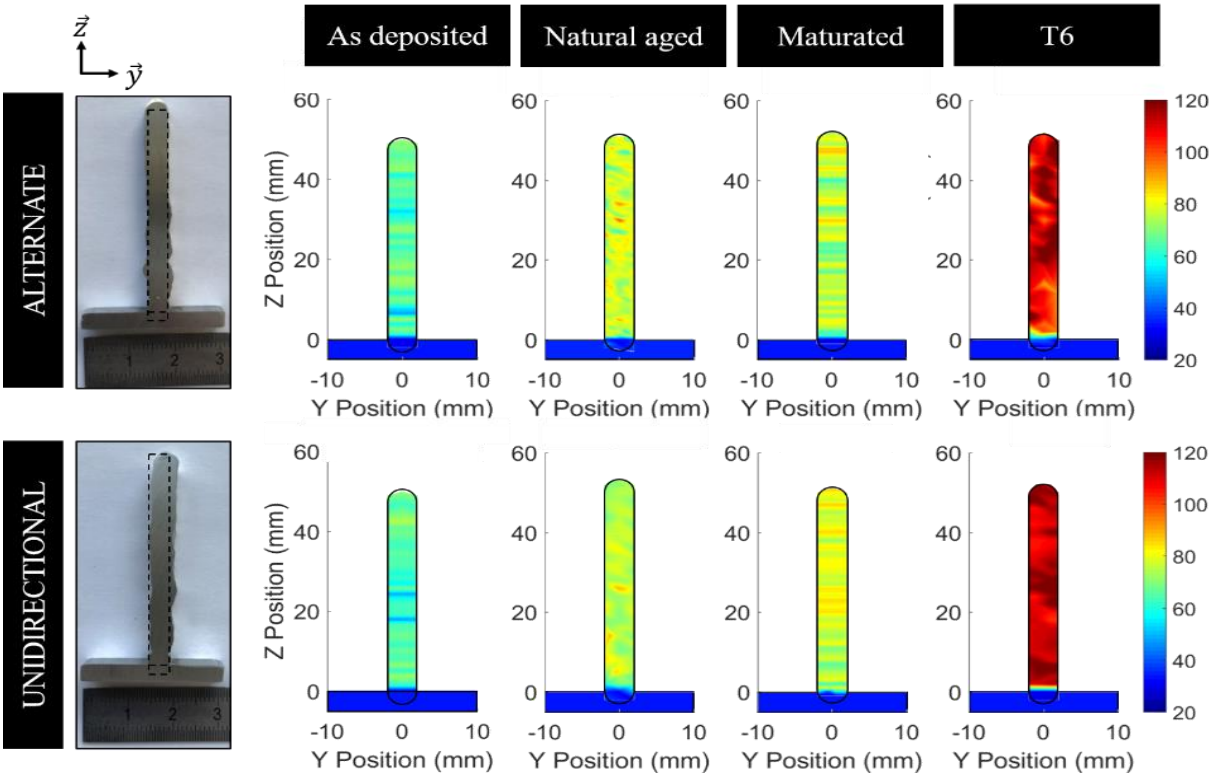

Figure 5: Hardness mapping for the two strategies and different metallurgical states

The deposition strategies seem to lead to the same hardness values. The different temperature gradients, solidification rates as well as the complex thermal effects which appear during the process seem to have no influence on the hardness values of each layer. Due to the material high thermal conductivity and the time between layers, it is possible that the last layer leads to homogenise the metallurgical state giving rise to a homogeneous hardness. Table 2 gives a summary of the hardness of the built material in the different metallurgical states investigated in this work.

Table 2: Hardness properties for the different heat treatments and deposition strategies

Metallurgical State	As deposited		Naturally aged (2 weeks /RT)		Maturated (2h/90°C)		T6 (530°C/1h + 175°C/8h)	
Strategy	Alternate	Unidirectional	Alternate	Unidirectional	Alternate	Unidirectional	Alternate	Unidirectional
Maximum hardness ($HV_{0.1}$)	75	73	100	89	88	100	137	140
Mean hardness ($HV_{0.1}$)	64	64	80	75	78	76	124	118
Minimum hardness ($HV_{0.1}$)	48	48	49	53	62	49	112	100
Standard deviation ($HV_{0.1}$)	5	6	10	6	5	9	6	6

As a result, for a given heat treatment the two strategies give the same hardness. As-deposited material has an average hardness of 64 $HV_{0.1}$ approaching the hardness found for the quenched material. The deposited material is probably quenched due to the high cooling rates. Indeed, it goes from liquid temperature to ambient temperature in few seconds. The other successive layers are rapidly deposited and the time spent in the high to moderate temperature range is brief. Thus, the alloying element mobility is not sufficient to precipitate hardening phases. The as-deposited part is in the solutionized state. Therefore, hardness is low because the only hardening mechanism present in this case is the solid solution strengthening. Naturally aged material, obtained after two weeks at room temperature, has an average hardness of 75 $HV_{0.1}$ corresponding to the value found for the T4 state. A forced maturation heat treatment of 2 hours at 90°C did not allow to modify the hardness further, highlighting that metallurgical stability is reached in the material after the natural ageing. Lastly, the T6 heat treatment carried out on the walls leads to higher hardness (124 $HV_{0.1}$ for the alternate strategy and 118 $HV_{0.1}$ for the unidirectional strategy) than that obtained on forged material (equal to 107 $HV_{0.1}$ according to ASM standard [55]). The unidirectional strategy gives a hardness close to the alternate one. It lies within the dispersion of measurements (5 to 10 $HV_{0.1}$).

3.5. Microstructural characterization

3.5.1 Microstructure and macrostructure observations by optical microscopy

As illustrated in Figure 6 (a), two types of microstructures are revealed: columnar and equiaxed grains with OM. Both deposition strategies induce the same stacking structure of alternate layers of equiaxed and columnar grains. The substrate (i.e. the baseplate) can be considered as equiaxed. Each layer in the built walls is constituted of columnar grains growing from the bottom of the layer with, on top, a finer layer of equiaxed grains as schematised on Figure 6 (a). Each new built layer partially melts the previous one. The characteristic depth of the remelted layer has been measured around 200 µm. The measurements of the heat-affected zones and molten zones were determined during a test campaign in which different settings were studied. A first measurement was carried out on a single layer and then on 2, 3, 4, 5, 7 and finally 10 layers. Analysis of heat-affected zones and molten zones have been achieved thanks to optical microscope on chemically attacked polished cross-cut samples. Due to the low heat input produced by the CMT technology, only a very narrow heat affected zone of about 10 µm in depth is present where a very slight grain coarsening is observed.

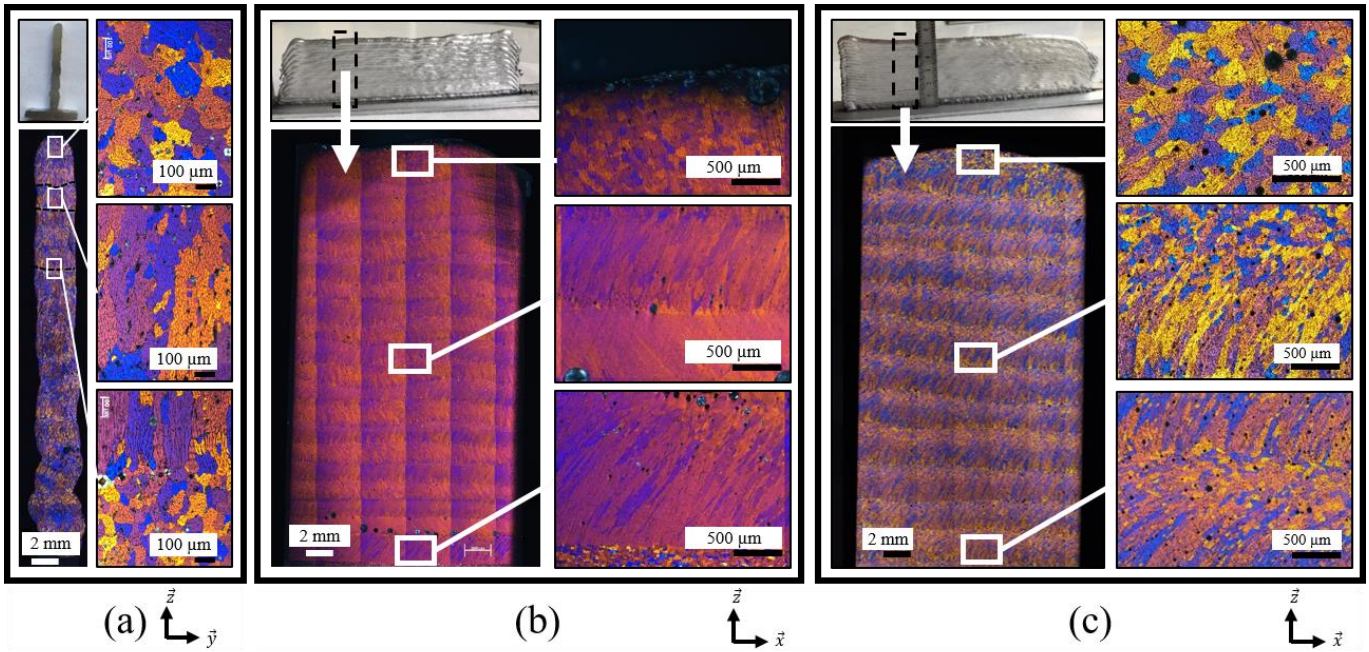

Figure 6: Macrographs illustration of the microstructure for the as-deposited WAAM AA6061 with magnification of enclosed regions by the white square for : (a) longitudinal section similar for both strategy, and in the X-Z plane section for (b) alternate strategy, (c) unidirectional strategy.

The same observations have been made on longitudinal-sections (plane X-Z) on samples cut from the wall thickness. Such an observation of a sample built with the alternate strategy is presented in Figure 6 (b) while Figure 6 (c) displays it for a sample produced with the unidirectional. Although the two strategies give similar microstructures in cross-section, they influence the direction of the columnar-grain growth in the longitudinal plane. Indeed, the growth direction of the columnar grains is linked to the welding direction (via the heat gradient developing during the welding operation). Thus, the alternate strategy (Figure 6 (b)) - alternating between two opposite welding directions - produces columnar grains which grow along two directions of solidification symmetrical to the transverse plane (Y-Z). The unidirectional strategy (Figure 6(c)) retains the same solidification direction layer after layer. For both strategies, the equiaxed grain proportion seems to be equivalent in terms of size distribution. These microstructural observations in the X, Y and Z directions allow to evaluate the morphology of the grains. In the first instance, the grain size is measured according to the intercept method presented in the ASTM E112 standard [56]. The use of this method is the most appropriate to evaluate the size of the columnar grains as well as their aspect ratio. As detailed in this standard, the three main measurement directions have been identified. The mean lineal intercept length $\bar{l}$, for columnar grains, is obtained from the equation (1).

$$\bar{l} = \sqrt[3]{\bar{l}_L . \bar{l}_T . \bar{l}_P} \quad (1)$$

Where $\bar{l}_L$, $\bar{l}_T$ and $\bar{l}_P$ are the mean lineal intercept length on the longitudinally, transversely and planar oriented surface, respectively. For equiaxed grain structure, the grain size is obtained more directly through the mean lineal intercept length. Measurements in the longitudinal plane are reported in Table 3.

Table 3: Measurements obtained by the intercept method.

Strategy	Zone	Mean Intercept (µm) Longitudinal	Mean Intercept (µm) Transverse	Mean Intercept (µm) Planar	Mean Intercept (µm)	Aspect Ratio (L/T)
Unidirectional	Equiaxed	/	/	/	95	1.0
	Columnar	464	99	93	163	4.7
Alternate	Equiaxed	/	/	/	86	1.0
	Columnar	319	99	93	143	3.2

Results on average area, diameter and size of grains for the two sets of grain population (equiaxed and columnar), determined according to ASTM E112 standard test methods for the different deposition strategies, are summarized in Table 4.

Table 4: Results calculated from measurements in Table 3 according to the ASTM E112 standard test's methods.

Strategy	Zone	Average Grain Area (µm²)	Average Diameter (µm)	Grain size n° (G)
Unidirectional	Equiaxed	11405	107	3.5
	Columnar	32258	180	2.0
Alternate	Equiaxed	9735	98	3.7
	Columnar	19056	142	2.7

Concerning the equiaxed areas, whatever the strategy being used, the grain size remains very similar around 100 µm. However, considering the columnar grains, these measurements show that the unidirectional strategy produces slightly longer grains than the alternate one, the mean intercept in the two perpendicular directions being almost equal for both strategies, leading to an aspect ratio of 4.7 for the unidirectional strategy and 3.2 for the alternate one.

3.5.2 EBSD Analysis

Grain size, shape and crystallographic distributions have been evaluated through EBSD and compared with the OM measurements. EBSD inverse Pole Figure (PF) maps and PF measured on samples built using each strategy are presented in Figure 7. They corroborate the previous analysis and provide additional information.

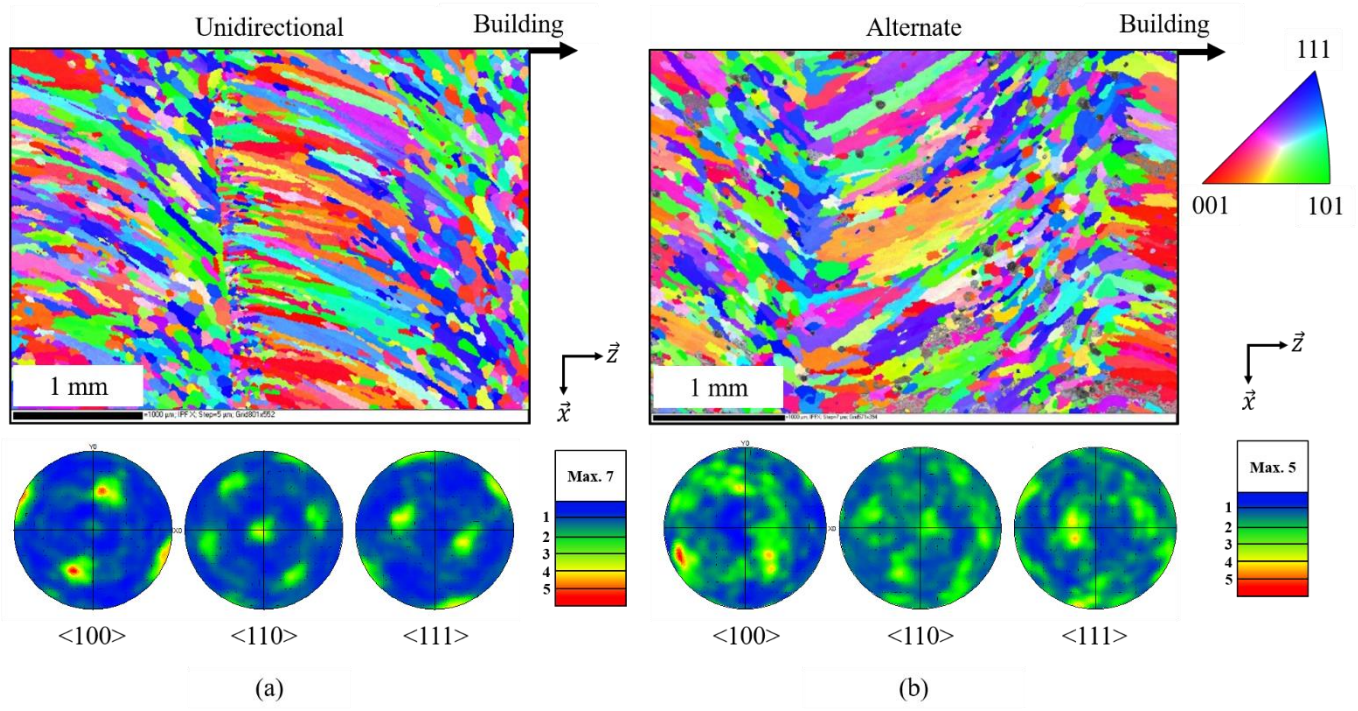

Figure 7: Grain morphology and crystallographic texture for the (a) unidirectional strategy and (b) alternate strategy.

Whatever the strategy, deposited parts are composed of two alternate microstructure zones: equiaxed and columnar dendritic grains. This hierarchical stacking of grains morphologies can explain the narrow distribution of microhardeness values along the Z axis as seen on Figure 5. It may be noted that the columnar grains are elongated along the solidification direction and have a significant aspect ratio (see Table 4). These grains grow in epitaxy on the previous layer so they did not go through a nucleation stage. This phenomenon occurs because each layer has the same composition and the same crystallographic structure. Growth can then occur spontaneously without requiring activation energy as soon as the temperature drops below the liquidus [57,58]. The phenomenon of competitive growth explains the preferential grain growth direction leading to the columnar shape of the grains. This appears

during solidification in polycrystalline materials with dendrites with various crystallographic orientations. Some dendrites have preferred growth orientations at the liquid / solid interface along the maximum heat flow direction. The favoured growth direction depends on the crystal structure, this direction for face-centred cubic (FCC) materials, as aluminium based alloys, is <100> [57,59]. The unidirectional strategy gives a single grain growth direction causing a sharp crystallographic <100> texture in the direction X+65° as illustrated in the PF in Figure 7(a). The alternate strategy gives a more balanced texture with two preferential solidification directions (Figure 7(b)). As shown in Figure 8(a), the n layer displays a marked <100> texture component in the X+65° direction while the n+1 layer shows a <100> texture component with the same intensity in the X-65° direction. Therefore, while the overall texture obtained with the alternate strategy seems more homogeneous, we can observe that each layer exhibits a strong <100> crystallographic orientation enhancement.

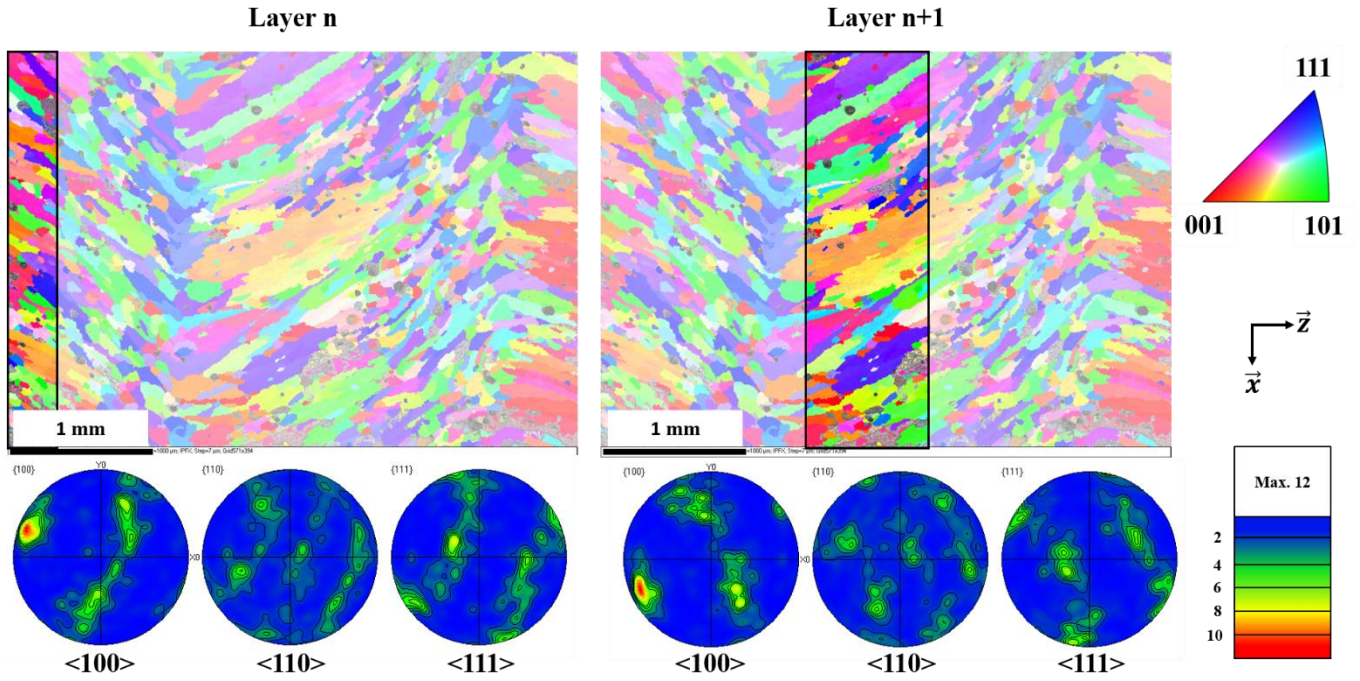

Figure 8: Texture evolution (a) layer n, (b) layer n+1.

The grain morphologies determined using EBSD correspond to the results obtained with OM. The observed grain size distributions determined for both deposition strategies are presented in

Figure 9 as a histogram. One can see that the alternate strategy produces a higher proportion of fine grains than the unidirectional one. A closer look at grains with an equivalent diameter larger than 15 µm, shows that the unidirectional strategy produces more of those large grains. Although coherent, the average grain sizes observed by the EBSD technique are much smaller than those observed by OM. This may be explained by the fact that very small grains of size less than 2 µm, which are not measurable with OM technique, were considered for the determination of size distributions by EBSD. In addition, EBSD results may also be affected by preparation artefacts and indexation errors.

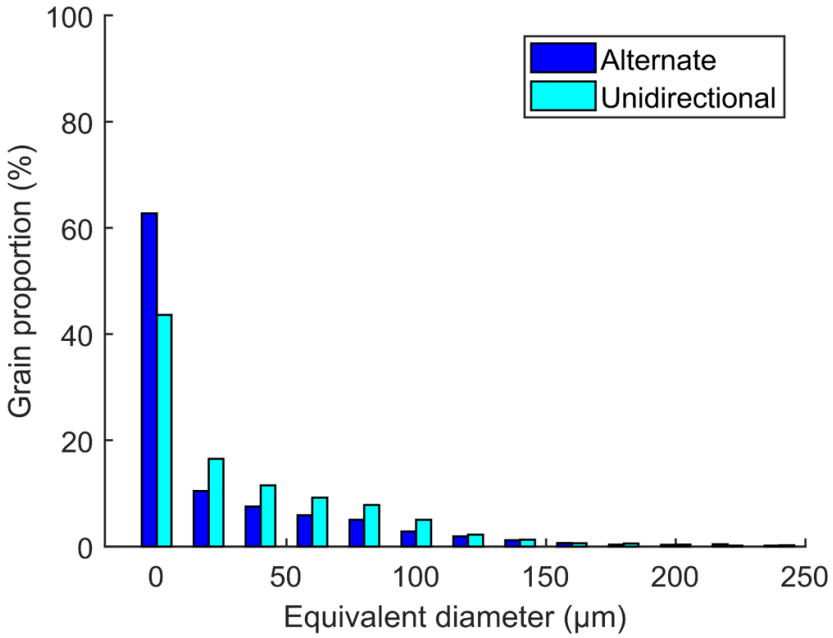

Figure 9: Grain size histogram obtained by EBSD

The deposition conditions promoted the formation of an equiaxed grain layer at the top of each deposited layer. The heterogeneous nucleation leading to this equiaxed layer may stem from constitutive phases that are able to remain unmelted and form the non-dendritic equiaxed zone. It may also stem from torn out arms of dendrites. Indeed, due to high welding speed, important liquid flow in the melting pool is emerging which can sweep dendrite branches away [60]. These dendrite arms, torn out from the dendrites by important liquid flow within the melting pool, can serve as heterogeneous nucleation sites for the growth of new grains with random orientations in the rapid cooling top layer of liquid. Therefore, equiaxed grains can be found at the top of each layer. In the present study, dispersoids or constitutive phases have been rarely found at the centre of the equiaxed dendritic grains on the cross-sections. The assumption of the dendrite arm detachment should therefore not be ruled out. It is also possible that the two phenomena are both participating to the formation of these equiaxed grains. Equiaxed grain layer ensures a large amount of grain boundary surfaces, hence reducing the hot cracking formation. Thus, their presence is most likely responsible for the absence of hot cracking in the WAAM 6061 aluminium alloy. An alternative assumption, explaining the hot cracking absence, is that the CMT process enables the rapid filling of the inter-dendritic spaces, fast enough to accommodate the stresses applied during the cooling of the weld bead.

3.5.3 Micrometric phases (intermetallic and β-phase)

Micrometric phases have been studied through SEM observations. Back-Scattered Electrons (BSE) contrast is strongly related to the mean atomic number of the irradiated zone. Therefore, it enables to highlight the presence of composition variations at a scale down to a few hundred of nanometres. These composition variations in metallic alloys are usually due to the presence of secondary phases distributed within the material matrix. As we can see in Figure 10, two minor phases are present in the additive manufacturing AA6061-wire, a globular dark-grey phase and a more polygonal white phase. We have measured the composition of one precipitate of each of these minor phases using local EDS analysis (Figure 10(a)), whose results are displayed on the diagram presented in Figure 10(b). Their compositions enable to identify the two types of observed minor phases: the globular dark-grey phase is the β-phase (Mg_2Si) and the more polygonal white phase rich in Fe and Si is an iron InterMetallic phase (IM).

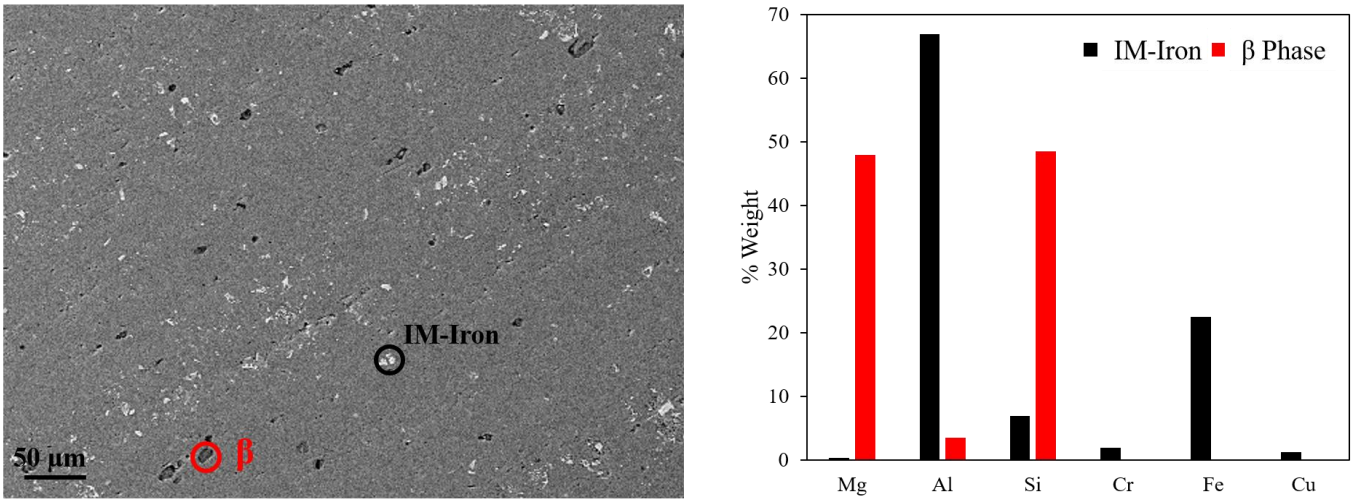

Figure 10: (a) SEM image with BSE contrast. (b) EDS of β-phase (red) and iron-IM (black).

The SEM images in BSE contrast in Figure 11, shows the AA6061 alloy at different metallurgical states being: (a) before the WAAM (wire), (b) as-deposited and (c) after an additional T6 heat treatment. In the wire filler, the microstructure is similar to the one found for conventional forged AA6061. The globular dark-grey β-phase and the polygonal white iron-rich IM phases are both present. In the as-deposited material, a silicon-rich phase network is observed in light-grey. This network is formed in interdendritic spaces and has already been deeply studied in the foundry field [63]. β-phase is also observed in proportion and in size equivalent to that observed in the wire. The T6 heat treated material no longer presents the previously observed network of Si-rich phase. In addition, all the intermetallic and β-phase are fewer and smaller than those found in the wire and the as-deposited material.

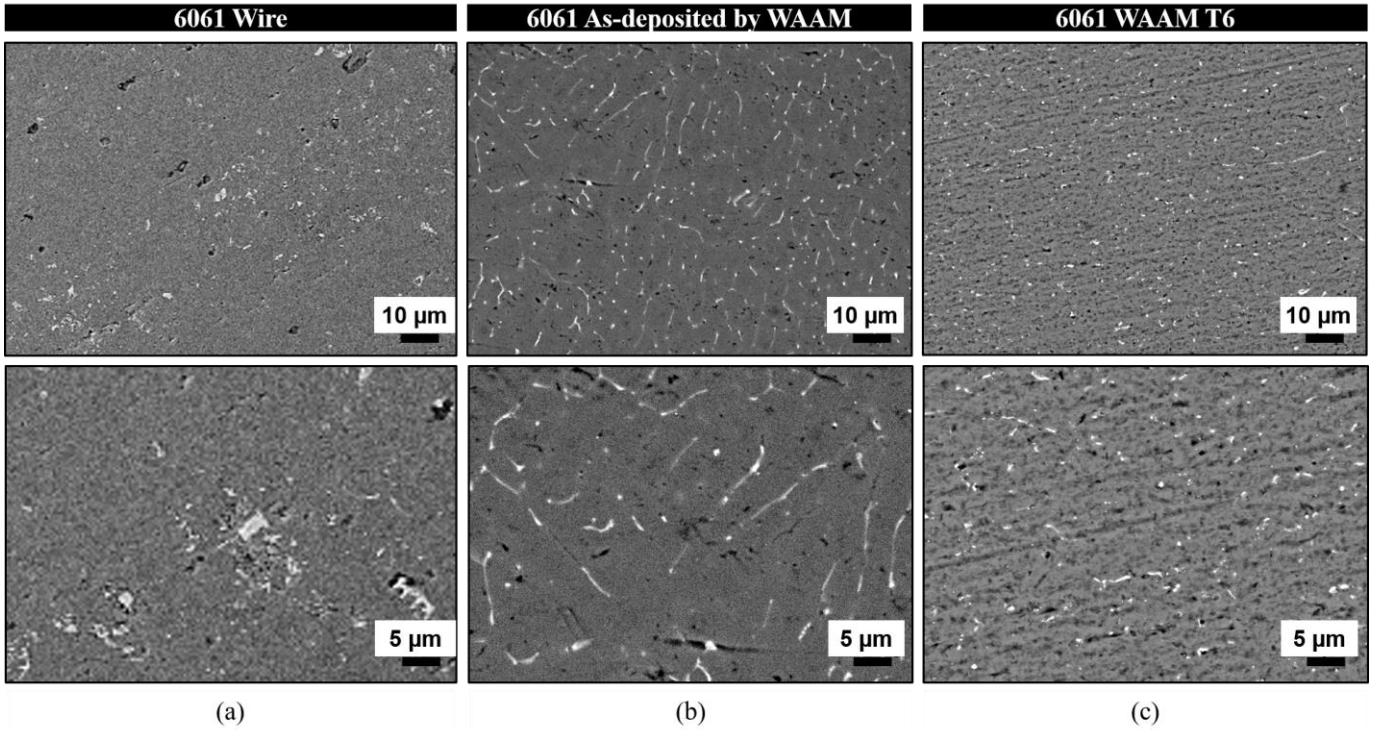

Figure 11: AA6061 at different metallurgical states (a) wire filler, (b) WAAM as-deposited material, (c) T6-treated WAAM material.

Two main precipitated phases are commonly found in AA6061 [69]:

- Coarse β-Mg_2Si precipitates are formed during the cooling of the alloy and dissolved thanks to the stages of homogenisation/solutionizing heat treatment. However, too slow quenching after solutionizing results in heterogeneous precipitation of this phase at the grain boundaries. Due to their large size and low number density, these precipitates do not take part in the structural hardening of the alloy. Precipitation of coarse β particles even contributes to the limitation of Al-Si-Mg alloys hardening since it decreases the amount of Mg and Si available for nanoscale precipitation of the hardening nanophases [69].
- Iron-rich intermetallic (IM) phases are characterised by the presence of iron. The α_c-$Al_{12}(Fe_xMn_{1-x})_3Si$ phases are formed during the homogenisation heat treatment. In a similar way, as the β precipitates, iron-IM are coarse and then do not participate directly to the material hardening [69].

After a T6 heat treatment, the silicon-rich phase network is no longer visible and micrometric phases (iron-IM and β-phase) are smaller and fewer than in the wire. The iron-IM and β-phase have probably been melted within the electric arc during deposition and, due to the extremely high cooling rate and the induced rapid solidification, new particles could not nucleate and grow significantly. Due to very low solubility in solid aluminium, iron segregates within the interdendritic spaces (solidified last drops of liquid). After the T6 heat treatment – and especially after its first step of solutionizing –, Fe becomes more homogeneously distributed within the material, and all the β-phase precipitates have been dissolved in the α-Al matrix. α-Al matrix, enriched with alloying elements, could significantly change the precipitation kinetics leading to different precipitation states after T6 heat treatment [70].

3.6. Hardened precipitates characterization

AA6061 is an age hardening aluminium alloy, its high mechanical properties stem thus from its precipitation state. Therefore, minor phase nature, spatial and size distributions play an important role. These phases appear during a controlled heat treatment - to master these three aforementioned factors - and are widely influenced by the alloy composition and its thermomechanical history. However, additively manufactured parts undergo a complex thermal history possibly altering the alloy composition (i.e. vaporisation as seen in 3.2) and causing the evolution of the micrometric and nanometric precipitated phases. Hence, it is important to investigate the nature, the localization and the size of these minor phases present in AA6061 additively manufactured parts and their evolution during subsequent heat treatments.

The nanometric precipitates have been observed by TEM. Specimens have been cut out from the middle region of the parts built by WAAM. The same precipitation state has been observed in the parts produced using both building strategies. Thus, we report in this paper results obtained from samples built using only the alternate strategy. Even if the nanostructures in AA6061 produced by traditional route of forging have been the subject of numerous works [9,47,69], an AA6061 sheet in the T6 state stemming from this route has also been studied as a reference to compare with. Two main types of precipitates have been observed: dispersoids and nanometric phases (β'', Q', L…).

3.6.1 Dispersoids

Dispersoids are incoherent with the matrix. They have a characteristic length in the range of 10 to 500 nm and a spherical or parallelepipedal morphology. Figure 12 shows bright-field TEM images of dispersoids for (a) the T6 forged material (reference), (b) the as-deposited WAAM material and (c) the T6 WAAM material.

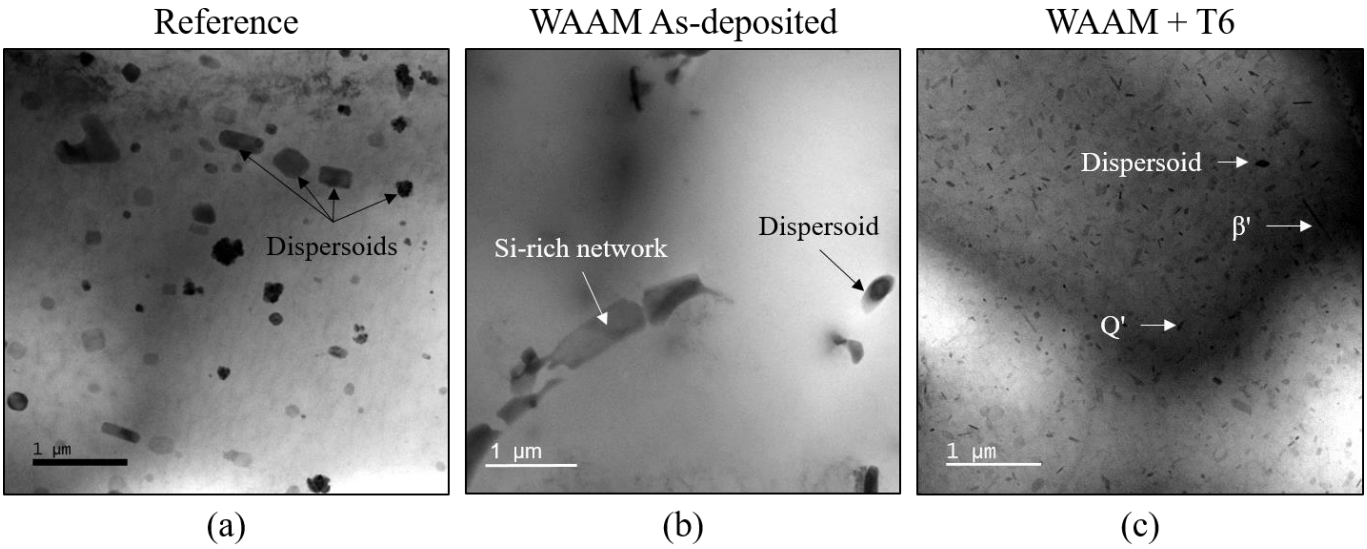

Figure 12: Bright-field TEM images of dispersoids for (a) the forged material at T6 state taken as the reference, (b) the WAAM material as-deposited and (c) the WAAM material at T6 state.

The observation of the T6 forged material (Figure 12(a)) highlights the presence of dispersoids with various sizes and shapes. These dispersoids are coarse (60 - 600 nm), incoherent with the matrix and homogeneously dispersed within the grains. Figure 12 (b) shows a bright-field TEM image of the as-deposited WAAM material. One can observe the segregation of a Si-rich phase along the grain boundaries, part of the Si-rich phase network presented in section 3.5. It could be noted the presence of very large dispersoids with a rather low number density, way lower than the one observed in the reference material. As explained earlier, this phenomenon is encountered when long soaking durations at rather high temperatures are undergone by the material. Additively manufactured material underwent temperatures up to 400°C, which could explain the presence of large dispersoids with low number density. In Figure 12 (c), we observe smaller dispersoids in the T6 WAAM material. They are in lower quantity and their shape are still widely varying. Other small phases appear: large β'-phase and coarse Q'-phase are observed. The characteristics of those phases are presented in section 3.6.2.

Dispersoids are usually formed during the homogenisation heat treatment, their size varies depending on its duration and temperature [77]. Indeed, higher temperatures and longer holding times promote their size to increase and their number density to decrease [78]. Although the primary function of dispersoids is to improve fracture toughness by limiting grain growth, this type of precipitates has a rather limited direct effect on the alloy strengthening [78,79]. Their effect on mechanical behaviour comes from the following phenomena: they may act as nucleation sites for β-particles (Mg_2Si) after homogenisation. Therefore, a high number density and a uniform size distribution of small β-particles lead to a better dissolution during further heat treatment prior to the final age hardening step [80]. High temperature (up to 400°C) are repetitively applied during WAAM process, which could explain the presence of large dispersoids. This configuration is not favourable to obtain suitable mechanical properties in terms of toughness. Prior to the homogenisation step of the T6 heat treatment, a uniform distribution of small dispersoids with high number density is preferred because this can lead to the precipitation of a higher volume fraction of strengthening particles after ageing step of the T6 heat treatment.

3.6.2 Nanometric phases

Nanometric β''-phases are the main hardening phases of the alloy. These precipitates, also called in the literature "GPII" [72], heterogeneously nucleate on GPI [81]. They are needle-shape of around 4 nm in diameter and up to 10 nm long [72]. The β" needles lie in the direction <001> of the aluminium matrix, and their number density, in the AA6061 T6, is around $10^{22}/m^3$ according to Flament [69]. The stoichiometry of the β"-precipitates, according to Zandbergen *et al.* [75], is Mg_5Si_6. This phase, in the form of small size precipitates coherent with the surrounding matrix and finely dispersed within the latter, is usually associated with the mechanical resistance peak of the AA6XXX. The temperature and the duration of the ageing heat treatment enabling these phases to be obtained is approximately 170°C for less than 10 hours (175 °C for 8 h is commonly used as heat treatment) [82]. Over-ageing

of the material would lead to the further transformation of the metastable β”-phase, mainly into the less metastable β’-phase, which is well documented [47]. The transformation of the β”-phase towards the β’-phase takes place at the very beginning of the transformation; these two phases coexist until the complete dissolution of the β’’-phase.

β’-precipitates have a rod shape with a characteristic dimension of its long axis of about 100 nm and contrary to the β’’-precipitates they are only semi-coherent with the matrix. Vissers *et al.* [72] determined their structure to be hexagonal and their stoichiometry to be Mg_9Si_5. This phase finally evolves during further over-ageing to form the stable FCC β-phase, of Mg_2Si stoichiometry. It results in rather large precipitates – platelets of micrometric characteristic size – with lower number density and incoherent with the surrounding matrix leading to the softening of the alloy. The latter can only be observed by orienting the crystal along the axis zone <001> [76], but since TEM enables only local characterisation, it is difficult to establish a statistic description of the size and volume fraction of these precipitates

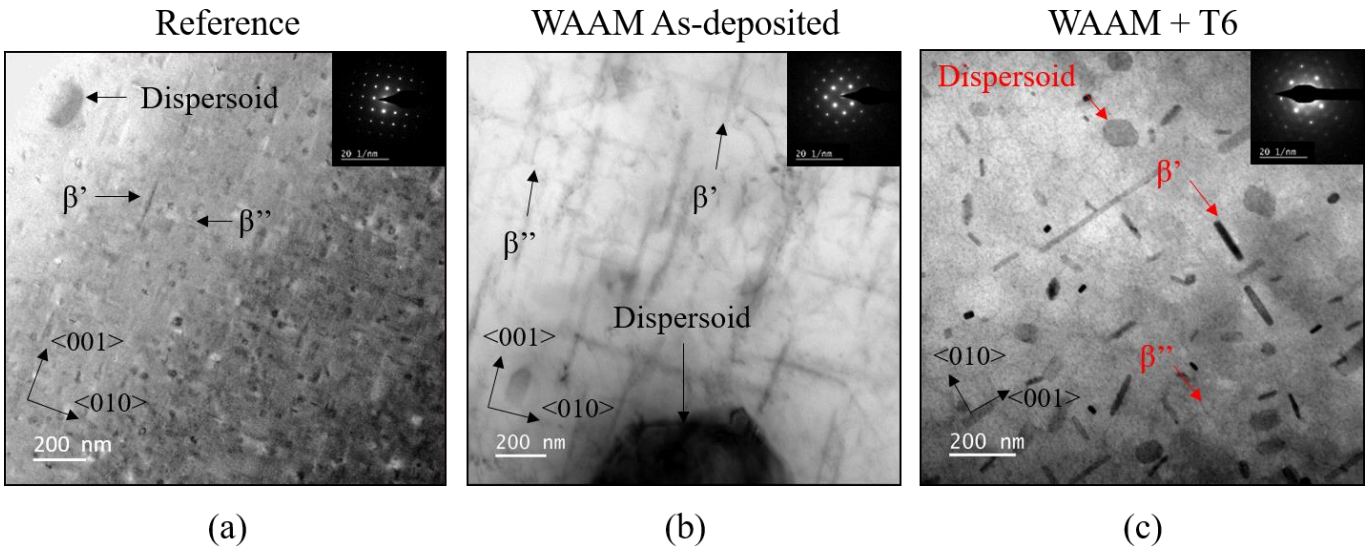

Figure 13: Bright-field TEM images of dispersoids, nanometric β’’ and β’ phases and associated diffraction pattern for (a) the forged T6 material taken as the reference, (b) the WAAM as-deposited material and (c) the WAAM T6 material.

The typical diameter of the precipitates is around 4 nm and their characteristic length is around 50 nm which is the usual size according to Vissers *et al.* [72]. β’-phase precipitates are more rarely found in this material condition. They are distinguished from the β’’-precipitates by their size: their diameter is above 10 nm and their length ranges between 100 and 500 nm according to Myhr *et al.* [70]. One can also found large dispersoids in the matrix, but no other phase is observed. Figure 13(b) shows the TEM image of the as-deposited material. β’’- and β’- precipitates are found nearby the large dispersoids. At a distance of 1 µm far from these large dispersoids, precipitates are no longer observed. β’’-precipitates have also been observed in the T6 WAAM material as shown in Figure 13(c)**.** Isolated precipitates were measured with High-Resolution TEM (HR-TEM). The obtained β’’-precipitates have a length set between 5 and 200 nm and a diameter between 2 and 10 nm. Simultaneous presence of large β’’-precipitates and β’-precipitates is the sign of a slight over-ageing undergone by the material. Even if the material is homogenised during the first step of the T6 heat treatment, the β’’-phase does not have the dimensions usually reported for the T6 material [72]. β’’-phase is not the only nanoscale phase present in the material. A broad range of metastable phases can be found in Al-Mg-Si-Cu alloys. These phases are formed from particular compositions in the T6 state and can coexist with β’’-phase [83,84]. L- and Q’- phases are observed in WAAM deposited material as illustrated in Figure 14. These phases are not found in the forged material (Figure 13) for the same heat treatment.

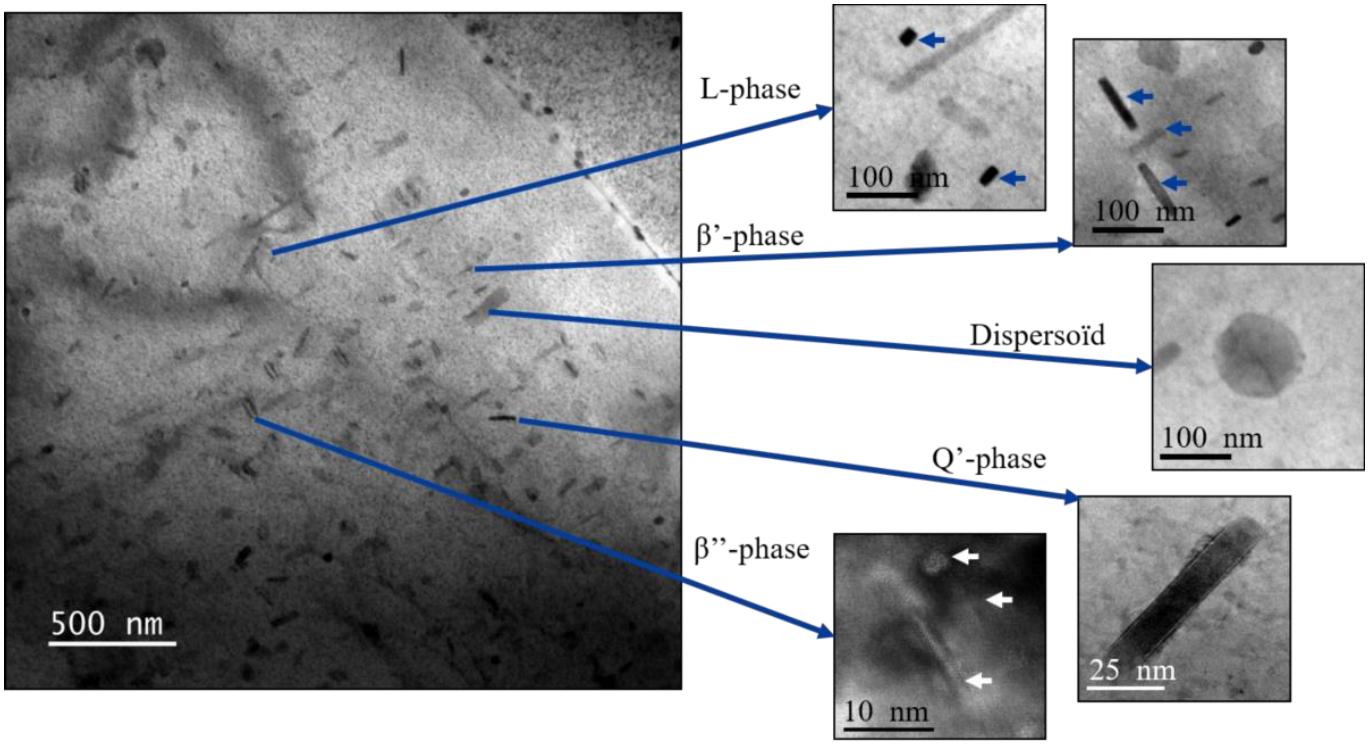

Figure 14: Bright-field TEM images of nanometric phases observed in the WAAM T6 material highlighting the presence of Q', L and β'' phases.

Hardening β-type precipitates have been studied, showing the coexistence of β''- and β'- phases. This may be due to compositional fluctuations (matrix enrichment of the alloying elements) as well as the complex thermal cycles applied during the process. In addition, the dispersoids being observed in the previous section are quite different as compared to the reference. Their size and volume fraction may influence the precipitation kinetics. These observations lead us to the conclusion that the conventional T6 treatment applied to the WAAM material resulted in a slight over-ageing of this material. L-phase is considered as a hardening phase and Q'-phase as a softening precipitate. It is therefore possible that the complex coexistence of these different phases (GPI, β'', β', L, Q', dispersoids, etc.) could induce significant hardening of the material. It is however difficult to clearly explain the formation mechanism as well as the role of each of these phases taken independently on the global mechanical behaviour.

3.7. Residual stress analysis

Residual stresses, developed during the building process, clearly have a significant influence on the mechanical performance and can lead not only to delamination from the supporting structures or unwanted shape distortion but also to early crack formation [85]. WAAM process develops large residual stresses depending on the material, the desired geometry and the clamping conditions. The origin of residual stresses is the non-uniform thermal contraction and expansion of the material during the different thermal cycles related to this process. In the literature, Coules *et al.* [86] describe the tensile residual stress formation in welded joints through material shrinkage phenomena that occur during the cooling. Several studies, focused on residual stresses within parts made by WAAM, are available [85,87,94]. As explained by Szost *et al.* [87], when molten metal is solidifying on a substrate, the thermal contraction generates tensile stresses in the deposited layer and compression stresses in the substrate. Additively manufactured structures consist of a layer-by-layer building, accumulating residual stresses within each layer. Therefore, high stress level can be obtained during the building process and trapped within the material as residual stresses. To understand the stress development, ND experiments have been carried out on SALSA beamline at ILL (see section 2.5). The measured average lattice strains within the diffracting volume are calculated from the Bragg's angle shift (Eq. (2)) based on the true (rational) strain definition [95]. For these experiments, the strain-free Bragg's angle, θ_0, is estimated through an averaging of θ values over the sample height in the three orthogonal directions X, Y and Z [94].

$$\varepsilon_{ii} = \ln\left(\frac{sin\theta_0}{sin\theta}\right) \qquad i = x, y, z \ (2)$$

This assumption, which supposes that the mean stress in the whole part is equal to zero, due to the residual stress equilibrium, does not consider a possible microstructure evolution. ND data was processed using the LAMP software [96] to obtain the peak positions. The correlation between residual normal stresses σ_{xx}, σ_{yy}, σ_{zz} and the 3 orthogonal measured lattice strains along the macroscopic coordinate axes is given by Eq. (3).

$$\sigma_{ii} = \frac{\left(2S_1(hk.l)+\frac{1}{2}S_2(hk.l)\right)}{\frac{1}{2}S_2(hk.l)\left(3S_1(hk.l)+\frac{1}{2}S_2(hk.l)\right)}\varepsilon_{ii} - \frac{S_1(hk.l)}{\frac{1}{2}S_2(hk.l)\left(3S_1(hk.l)+\frac{1}{2}S_2(hk.l)\right)}\sum_{j\ j\neq i}\varepsilon_{jj} \ (3)$$

$j = x, y, z$

$\frac{1}{2}S_2(hk.l)$ and $S_1(hk.l)$ are the X-ray Elastic Constants (XEC) [97]. They depend on the measured {hkl} reflection and consider the elastic anisotropy of the diffracting grain group. The XEC have been calculated from single-crystal elastic constants (c_{11} = 108.2 GPa, c_{12}= 60 GPa and c_{44} = 28.5 GPa [29]) using an elastic-self consistent model [98]. The calculated XEC values of $\frac{1}{2}S_2(hkl)$ and $S_1(hkl)$, necessary for the stress calculation, are:

$$\frac{1}{2}S_2(31.1) = 19.187\ 10^{-6}\ \text{MPa}^{-1},\ S_1(31.1) = -4.945\ 10^{-6}\ \text{MPa}^{-1}.$$

Figure 15 shows the residual stress profiles along the height of the wall in the longitudinal X, transverse Y and normal Z directions for each strategy.

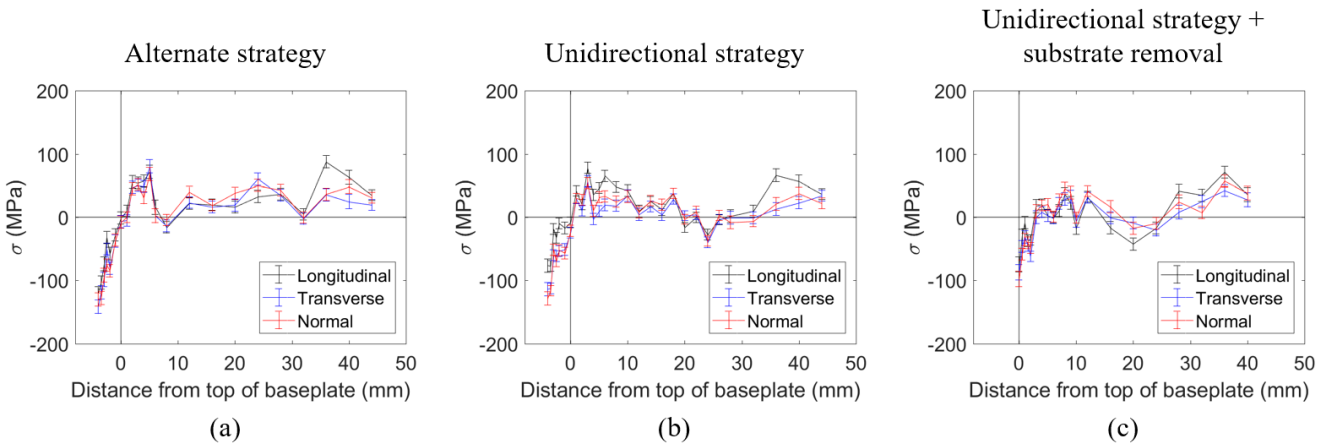

Figure 15: Evolution of the residual stresses along the height of the wall for each direction (longitudinal X, transverse Y and normal Z) within the samples built with (a) the alternate strategy ; (b) the unidirectional strategy and (c) the unidirectional strategy after substrate removal.

Alternate or unidirectional deposition strategies give similar stress levels and the same type of variations in all the three directions. Slightly higher stress levels are obtained in the longitudinal direction. This result has already been observed in the literature [23,85,87]. As shown in Figure 15, a global trend along the three directions is observed. Residual stresses are compressive with a maximum in the centre of the baseplate (z = -4 mm ; $\sigma_{ii} \approx$ -100 MPa). The residual stress increases rapidly toward tensile values with increasing z values. The highest normal stress values are obtained in the first layers (z = 4 mm ; $\sigma_{xx} \approx$ +90 MPa). A second maximum tensile stress is observed in the last layers (z = 40 mm ; $\sigma_{xx} \approx$ +80 MPa), remaining low in between.

Longitudinal direction follows the global trend. For alternate strategy, large compressive stresses (-129 MPa) are found in the middle of the baseplate (z = -4 mm) followed by maximum tensile stress (+80 MPa) in the first layers of the wall (z = 5 mm). The second maximum tensile stress is observed in the last layers (z = 37 mm ; +87 MPa). Unidirectional strategy also shows large compressive stresses (-116 MPa) in the middle of the baseplate (z = -4 mm) followed by maximum tensile stress (+78 MPa) in the first layers of the wall (z = 3 mm). The second maximum tensile stress is determined in the last layers (z = 36 mm ; +66 MPa). For both strategies, the transition zone between the baseplate and the wall is free from stress. Concerning the transversal direction, after a maximum reached at the beginning, tensile stress remains still globally low. To complete the description, one should precise that one single measurement point deviates significantly towards a high tensile stress in one case and toward a high compressive stress in the other. The mechanical properties of the specimen at ambient temperature have been characterised by

monotonic tensile tests: R_E = 189 ± 38 MPa (yield strength) and σ_{UTS} = 344 ± 43 MPa (ultimate tensile strength). In our study, stress level is always smaller than the yield strength of the samples: the stress component σ_{xx}= +/- 90 MPa (z = 4 mm) reaches 47% of the yield strength.

In order to reduce the residual stresses and depending on the part design and the overall desired aim, it is sometimes possible to remove the baseplate [87]. Hence, one sample was machined and removed from the baseplate to understand how it impacts the residual stress equilibrium. Figure 15 (c) shows the residual stresses in the sample produced with the unidirectional strategy after baseplate removal. A stress redistribution is then observed. The global trend found before baseplate removal shifts and a magnitude reduction is observed (i.e. z = 4 mm ; $\sigma_{xx} \approx$ +90 MPa before removal ; z = 4 mm ; $\sigma_{xx} \approx$ +49 MPa after removal). As found before substrate removal, similar stress levels and variations are found in all directions. From the first maximum compressive stress at the starting point (i.e. z = 0 mm ; $\sigma_{ii} \approx$ -87 MPa) , the residual stresses increase to reach a maximum tensile stress in the fourth layer (z = 8 mm ; $\sigma_{ii} \approx$ +45 MPa). The highest tensile stress is observed in the last layer (z = 36 mm ; $\sigma_{ii} \approx$ +57 MPa). After baseplate removal, a stress reduction up to 30% is observed.

Residual stresses developed during the building process have clearly an influence on the mechanical performance [85]. As explain by Szost *et al.* [87], a general trend, for which stresses are rather tensile in the wall and compressive in the baseplate, is usually found for the stress state reached after deposition. Once unclamped, the component tends logically to contract at the top and expand at the bottom. For this reason, bending takes place together with a stress redistribution. According to Martina *et al.* [85], during stress redistribution, stress magnitude decreases along the height of the building and can even become compressive at the top. The stress in the baseplate also evolves in the opposite way until being tensile at the bottom of the baseplate. Residual stress measurements show that alternate or unidirectional deposition strategies give similar stress levels and the same kind of variations in all measurement directions. Slightly higher stress levels are obtained in the longitudinal direction, which have already been observed in the literature [23,85,87,94]. The stress is generally maximal in the longitudinal direction and minimal in the transversal one where less matter restrains the geometry to deform [85,87,94]. A global trend along the three directions is observed. The residual stress passes through a maximum compressive stress at the centre (≈ -100 MPa) of the baseplate, then a maximum tensile stress is encountered in the first layer (≈ +90 MPa). A second maximum tensile stress is observed in the last layers (≈ +80 MPa), remaining low in between these two zones. The low stress magnitudes found are consistent with those reported by Hönnige *et al.* [23] on a AA2319 with CMT pulsed advanced deposition process. However, the global trend described by these authors seems to be different and the stresses in the transverse and normal directions are much lower than the values obtained in the present study. No element from literature and performed analyses enables us to explain this variation. Several studies, focused on residual stresses within parts built by WAAM, relate significant stress levels and distortions strongly depending on the material, the process parameters, the geometry and the clamping conditions [23,85,87–94]. It could be noticed that our results are not in agreement with these studies. But it should be also noted that the comparison with these works is very difficult since the process parameters and materials are not equivalent. The stress magnitude reduction of approximately 30% when the substrate is removed is however consistent with the literature [87].

CONCLUSIONS

From this experimental study, the following observations and conclusions can be drawn:

- It is possible to build parts free from significant defects with the AA6061 using the WAAM process. A very limited quantity of porosities is found thanks to a careful cleaning of the wire and substrate. Hot cracking can be avoided by the formation of equiaxed grains on the top portion of each deposited layer. This phenomenon is promoted by the presence of constitutive phases within the wire filler material and by the use of a high welding speed.
- The as-deposited material is quenched due to the rapid cooling of the deposit. During the holding step at room temperature, it undergoes natural ageing which leads to a relative metallurgical stability of the microstructure after two weeks, its hardness being then equivalent with the value obtained on the commercial T4 material. After a T6 heat treatment, the hardness value of the WAAM material is higher than the one measured on the commercial T6 material. This phenomenon can be explained by a state of precipitation

which is different from the one observed in the forged material, and more particularly, by the absence of large dispersoids and the coexistence of different phases (GPI, Q', β', β'', L) at the nanoscale.

- Both strategies produce stacked structures consisting of successive alternating layers of columnar and equiaxed grains. The as-deposited material shows a strong preferential crystallographic orientation, but less pronounced with the alternate deposition strategy. The micrometric phases found in the filler wire (iron-IM and β-phase) may be melted during the deposition process and are then no longer present in the deposited material. This variation changes the material concentration, containing more solutes that affect the precipitation kinetics obtained during the hardening T6 heat treatment, leading to a WAAM material harder than the usual material in the T6 state.
- TEM analyses have highlighted significant differences between the forged material and the WAAM material. At T6 state, there are no large dispersoids. However, it reveals a multitude of β'-, L-, Q'- and β''- phases in the material. This coexistence could explain the improvement of hardness properties.
- Finally, the stress analysis shows that both manufacturing strategies lead to similar stress profiles. Compressive stresses are found in the baseplate and residual tensile stresses along three orthogonal directions in the walls. Substrate removal reduces by 30% the maximum compressive stress.

Declaration of Competing Interest

The authors declare that they have no competing financial interests or personal relationships that could have appeared to influence the work reported in this paper.

Acknowledgments

This work is based upon experiments performed at the SALSA instrument (ILL, Grenoble, France). The authors thank the ILL neutron Facilities scientific comities for the allocated experimental days (experiment 81346).

Funded by the French Contrat Plan État-Région and the European Regional Development Fund of Pays de la Loire, the CIMEN Electron Microscopy Centre in Nantes is greatly acknowledged.

References

[1] T. Caffrey, T. Wohlers, R.I. Campbell, 3D Printing and additive manufacturing state of the industry annual worldwide progress report, Wohlers Assoc. (2016).

[2] A. Benoit, Soudage à l'arc semi-automatique (MIG / MAG), Tech. l'ingénieur Assem. des matériaux par soudage. 33 (2015) 14.

[3] S. Jacono, Quality of gas metal arc welds for rapid prototyping and wear replacement, Thèse de doctorat, University of Wollongong, 1999. https://ro.uow.edu.au/theses/2525.

[4] T. DebRoy, H.L. Wei, J.S. Zuback, T. Mukherjee, J.W. Elmer, J.O. Milewski, A.M. Beese, A. Wilson-Heid, A. De, W. Zhang, Additive manufacturing of metallic components – Process, structure and properties, Prog. Mater. Sci. 92 (2018) 112–224. https://doi.org/10.1016/j.pmatsci.2017.10.001.

[5] ASTM International, F2792-12a - Standard Terminology for Additive Manufacturing Technologies, Rapid Manuf. Assoc. (2013) 10–12. https://doi.org/10.1520/F2792-12A.2.

[6] C.R. Cunningham, S. Wikshåland, F. Xu, N. Kemakolam, A. Shokrani, V. Dhokia, S.T. Newman, Cost Modelling and Sensitivity Analysis of Wire and Arc Additive Manufacturing, Procedia Manuf. 11 (2017) 650–657. https://doi.org/10.1016/j.promfg.2017.07.163.

[7] C.M.A. Silva, I.M.F.. Bragança, A. Cabrita, L. Quintino, P.A.F. Martins, Formability of a wire arc deposited aluminium alloy, J. Brazilian Soc. Mech. Sci. Eng. 39 (2017) 4059–4068. https://doi.org/10.1007/s40430-017-0864-z.

[8] P. Kazanas, P. Deherkar, P. Almeida, H. Lockett, S. Williams, Fabrication of geometrical features using wire and arc additive manufacture, Proc. Inst. Mech. Eng. Part B J. Eng. Manuf. 226 (2012)

1042–1051. https://doi.org/10.1177/0954405412437126.

[9] H.S. Hasting, A.G. Frøseth, S.J. Andersen, R. Vissers, J.C. Walmsley, C.D. Marioara, F. Danoix, W. Lefebvre, R. Holmestad, Composition of β″ precipitates in Al-Mg-Si alloys by atom probe tomography and first principles calculations, J. Appl. Phys. 106 (2009) 123527. https://doi.org/10.1063/1.3269714.

[10] S. Kou, Welding Metallurgy, Weld. Metall. (2002) 353–374. https://doi.org/10.1002/0471434027.

[11] A. Benoit, Développement du soudage MIG CMT pour la réparation de pièces aéronautiques. Application aux pièces en alliage base aluminium 6061, Thèse de doctorat, Université de Nantes, 2012.

[12] D.E.J. Talbot, P.N. Anyalebechi, Solubility of hydrogen in liquid aluminium, Mater. Sci. Technol. (United Kingdom). 4 (1988) 1–4. https://doi.org/10.1179/mst.1988.4.1.1.

[13] W.R. Opie, N.J. Grant, Hydrogen solubility in aluminum and some aluminum alloys, Jom. 2 (1950) 1237–1241. https://doi.org/10.1007/bf03399138.

[14] Alcotec Corporation, Alumminium Filler Alloy - Selection Chart, (2015). https://www.google.com/url?sa=t&rct=j&q=&esrc=s&source=web&cd=1&ved=2ahUKEwjaksTv3MzoAhVZ5eAKHW_ZDwQQFjAAegQIAhAB&url=http%3A%2F%2Fwww.alcotec.com%2Fus%2Fen%2Fsupport%2Fupload%2FAluminum_Filler_Alloy_Selection_Chart.pdf&usg=AOvVaw3SDCY2tzEeX-POoNcn_jMv.

[15] M.F. Ahmad Ibrahim, S.R.S. Bakar, A. Jalar, N.K. Othman, J. Sharif, A.R. Daud, N.M. Rashdi, Effect of porosity on tensile behaviour of WELDED AA6061-T6 aluminium alloy, Appl. Mech. Mater. 66–68 (2011) 534–539. https://doi.org/10.4028/www.scientific.net/AMM.66-68.534.

[16] C. Galy, E. Le Guen, E. Lacoste, C. Arvieu, Main defects observed in aluminum alloy parts produced by SLM: From causes to consequences, Addit. Manuf. 22 (2018) 165–175. https://doi.org/10.1016/j.addma.2018.05.005.

[17] X. Fang, L. Zhang, H. Li, C. Li, K. Huang, B. Lu, Microstructure evolution and mechanical behavior of 2219 aluminum alloys additively fabricated by the cold metal transfer process, Materials (Basel). 11 (2018). https://doi.org/10.3390/ma11050812.

[18] J. Gu, B. Cong, J. Ding, S.W. Williams, Y. Zhai, Wire+Arc Additive Manufacturing of Aluminium, in: SFF Symp. Austin Texas, 2014: pp. 451–458.

[19] B. Cong, Z. Qi, B. Qi, H. Sun, G. Zhao, J. Ding, A comparative study of additively manufactured thin wall and block structure with Al-6.3%Cu alloy using cold metal transfer process, Appl. Sci. 7 (2017). https://doi.org/10.3390/APP7030275.

[20] J. Gu, J. Ding, S.W. Williams, H. Gu, P. Ma, Y. Zhai, The effect of inter-layer cold working and post-deposition heat treatment on porosity in additively manufactured aluminum alloys, J. Mater. Process. Technol. 230 (2016) 26–34. https://doi.org/10.1016/j.jmatprotec.2015.11.006.

[21] C.G. Pickin, S.W. Williams, M. Lunt, Characterisation of the cold metal transfer (CMT) process and its application for low dilution cladding, J. Mater. Process. Technol. 211 (2011) 496–502. https://doi.org/10.1016/j.jmatprotec.2010.11.005.

[22] M. Icardi, Wire + arc additive manufacturing (WAAM) for large scale components: aluminium alloys 2319 and 5554, Politecnico di torino, 2012.

[23] J.R. Hönnige, P.A. Colegrove, S. Ganguly, E. Eimer, S. Kabra, S. Williams, Control of residual stress and distortion in aluminium wire + arc additive manufacture with rolling, Addit. Manuf. 22 (2018) 775–783. https://doi.org/10.1016/j.addma.2018.06.015.

[24] J. Gu, J. Ding, S.W. Williams, H. Gu, J. Bai, Y. Zhai, P. Ma, The strengthening effect of inter-layer cold working and post-deposition heat treatment on the additively manufactured Al-6.3Cu alloy, Mater. Sci. Eng. A. 651 (2016) 18–26. https://doi.org/10.1016/j.msea.2015.10.101.

[25] F. Montevecchi, G. Venturini, N. Grossi, A. Scippa, G. Campatelli, Idle time selection for wire-arc additive manufacturing: A finite element-based technique, Addit. Manuf. 21 (2018) 479–486. https://doi.org/10.1016/j.addma.2018.01.007.

[26] A. Gomez Ortega, L. Corona Galvan, F. Deschaux-Beaume, B. Mezrag, S. Rouquette, Effect of process parameters on the quality of aluminium alloy Al5Si deposits in wire and arc additive manufacturing using a cold metal transfer process, Sci. Technol. Weld. Join. 23 (2018) 316–332. https://doi.org/10.1080/13621718.2017.1388995.

[27] Z. Qi, B. Cong, B. Qi, H. Sun, G. Zhao, J. Ding, Microstructure and mechanical properties of double-wire + arc additively manufactured Al-Cu-Mg alloys, J. Mater. Process. Technol. 255 (2018) 347–353. https://doi.org/10.1016/j.jmatprotec.2017.12.019.

[28] M. Köhler, S. Fiebig, J. Hensel, K. Dilger, Wire and arc additive manufacturing of aluminum components, Metals (Basel). 9 (2019) 1–9. https://doi.org/10.3390/met9050608.

[29] J. Gu, X. Wang, J. Bai, J. Ding, S. Williams, Y. Zhai, K. Liu, Deformation microstructures and strengthening mechanisms for the wire+arc additively manufactured Al-Mg4.5Mn alloy with inter-layer rolling, Mater. Sci. Eng. A. 712 (2018) 292–301. https://doi.org/10.1016/j.msea.2017.11.113.

[30] K. Oyama, S. Diplas, M. M'hamdi, A.E. Gunnæs, A.S. Azar, Heat source management in wire-arc additive manufacturing process for Al-Mg and Al-Si alloys, Addit. Manuf. 26 (2019) 180–192. https://doi.org/10.1016/j.addma.2019.01.007.

[31] Y. Yehorov, Exploring solutions to mitigate unidirectional grain growth and to set operational envelop for wire +arc additive manufacturing of aluminium alloys, Thèse de doctorat - Federal university of Uberlandia, 2018. https://doi.org/10.14393/ufu.di.2018.574.

[32] A. Horgar, H. Fostervoll, B. Nyhus, X. Ren, M. Eriksson, O.M. Akselsen, Additive manufacturing using WAAM with AA5183 wire, J. Mater. Process. Technol. 259 (2018) 68–74. https://doi.org/10.1016/j.jmatprotec.2018.04.014.

[33] B.F. Gomes, P.J. Morais, V. Ferreira, M. Pinto, L.H. De Almeida, Wire-arc additive manufacturing of Al-Mg alloy using CMT and PMC technologies, MATEC Web Conf. 233 (2018) 1–8. https://doi.org/10.1051/matecconf/201823300031.

[34] K. Derekar, J. Lawrence, G. Melton, A. Addison, X. Zhang, L. Xu, Influence of Interpass Temperature on Wire Arc Additive Manufacturing (WAAM) of Aluminium Alloy Components, MATEC Web Conf. 269 (2019) 05001. https://doi.org/10.1051/matecconf/201926905001.

[35] A. Elrefaey, Effectiveness of cold metal transfer process for welding 7075 aluminium alloys, Sci. Technol. Weld. Join. 20 (2015) 280–285. https://doi.org/10.1179/1362171815Y.0000000017.

[36] K.F. Ayarkwa, S.W. Williams, J. Ding, Assessing the effect of TIG alternating current time cycle on aluminium wire + arc additive manufacture, Addit. Manuf. 18 (2017) 186–193. https://doi.org/10.1016/j.addma.2017.10.005.

[37] K.S. Derekar, A review of wire arc additive manufacturing and advances in wire arc additive manufacturing of aluminium, Mater. Sci. Technol. (United Kingdom). 34 (2018) 895–916. https://doi.org/10.1080/02670836.2018.1455012.

[38] B. Wu, Z. Pan, D. Ding, D. Cuiuri, H. Li, J. Xu, J. Norrish, A review of the wire arc additive manufacturing of metals: properties, defects and quality improvement, J. Manuf. Process. 35 (2018) 127–139. https://doi.org/10.1016/j.jmapro.2018.08.001.

[39] A. Benoit, P. Paillard, T. Baudin, J.B. Mottin, Soudage homogène MIG de l'alliage d'aluminium 6061, MATEC Web Conf. 7 (2013). https://doi.org/10.1051/matecconf/20130702009.

[40] N.P. Kumar, S. Arungalai Vendan, N. Siva Shanmugam, Investigations on the parametric effects of cold metal transfer process on the microstructural aspects in AA6061, J. Alloys Compd. 658 (2016) 255–264. https://doi.org/10.1016/j.jallcom.2015.10.166.

[41] S. Selvi, A. Vishvaksenan, E. Rajasekar, Cold metal transfer (CMT) technology - An overview, Def. Technol. 14 (2018) 28–44. https://doi.org/10.1016/j.dt.2017.08.002.

[42] H.T. Serindag, Investigation of the Influence of Weld Defects on the Mechanical Behaviour of Cold Metal Transfer (CMT) and Cold Metal Transfer Pulsed (CMT-Pulsed) Arc Welded AA7075-T6 Al-Alloy Bu ..., (2019).

[43] G. Çam, G. İpekoğlu, Recent developments in joining of aluminum alloys, Int. J. Adv. Manuf. Technol. 91 (2017) 1851–1866. https://doi.org/10.1007/s00170-016-9861-0.

[44] Fronius international, CMT – Cold metal transfer: the cold welding process for premium quality, (2020). https://www.fronius.com/en/welding-technology/our-expertise/welding-processes/cmt.

[45] C.G. Pickin, K. Young, Evaluation of cold metal transfer (CMT) process for welding aluminium alloy, Sci. Technol. Weld. Join. 11 (2006) 583–585. https://doi.org/10.1179/174329306X120886.

[46] B. Mezrag, F. Deschaux-beaume, M. Benachour, B. Mezrag, F. Deschaux-beaume, M. Benachour, B. Mezrag, M. Benachour, Control of mass and heat transfer for steel / aluminium joining using Cold Metal Transfer process To cite this version : HAL Id : hal-01289341 Control of mass and heat transfer for steel / aluminium joining using Cold Metal Transfer process, (2016).

[47] C.D. Marioara, S.J. Andersen, H.W. Zandbergen, R. Holmestad, The influence of alloy composition on precipitates of the Al-Mg-Si system, Metall. Mater. Trans. A Phys. Metall. Mater. Sci. 36 (2005) 691–702. https://doi.org/10.1007/s11661-005-1001-7.

[48] S.J. Andersen, Quantification of the Mg2Si β″ and β′ phases in AlMgSi alloys by transmission electron microscopy, Metall. Mater. Trans. A. 26 (1995) 1931–1937. https://doi.org/10.1007/BF02670664.

[49] T. Pirling, G. Bruno, P.J. Withers, SALSA-A new instrument for strain imaging in engineering materials and components, Mater. Sci. Eng. A. (2006). https://doi.org/10.1016/j.msea.2006.04.083.

[50] Y.M. Zhang, Y. Chen, P. Li, A.T. Male, Weld deposition-based rapid prototyping: A preliminary study, J. Mater. Process. Technol. 135 (2003) 347–357. https://doi.org/10.1016/S0924-0136(02)00867-1.

[51] E.A. Brandes, G.B. Brook, Smithells Metals Reference Book: Seventh Edition, Smithells Met. Ref. B. Seventh Ed. (2013) 1–1800. https://doi.org/10.1016/C2009-0-25363-3.

[52] T. Yuan, Z. Yu, S. Chen, M. Xu, X. Jiang, Loss of elemental Mg during wire + arc additive manufacturing of Al-Mg alloy and its effect on mechanical properties, J. Manuf. Process. 49 (2020) 456–462. https://doi.org/10.1016/j.jmapro.2019.10.033.

[53] A. Block-Bolten, T.W. Eagar, Metal vaporization from weld pools, Metall. Trans. B. 15 (1984) 461–469. https://doi.org/10.1007/BF02657376.

[54] I. Arganda-Carreras, V. Kaynig, C. Rueden, K.W. Eliceiri, J. Schindelin, A. Cardona, H.S. Seung, Trainable Weka Segmentation: A machine learning tool for microscopy pixel classification, Bioinformatics. 33 (2017) 2424–2426. https://doi.org/10.1093/bioinformatics/btx180.

[55] ASM, Metals Handbook: Vol 2 - Properties and selection : Nonferrous alloys and special-purpose materials, ASM international, 1990.

[56] ASTM, ASTM E112-13: Standard test methods for determining average grain size, ASTM Int. (2013) 1–28. https://doi.org/10.1520/E0112-13.1.4.

[57] S. Kou, Welding Metallurgy, John Wiley & Sons, Inc., Hoboken, NJ, USA, 2003. https://doi.org/10.1016/S0016-7878(62)80017-0.

[58] A. Basak, S. Das, Epitaxy and Microstructure Evolution in Metal Additive Manufacturing, Annu. Rev. Mater. Res. 46 (2016) 125–149. https://doi.org/10.1146/annurev-matsci-070115-031728.

[59] G.P. Dinda, A.K. Dasgupta, J. Mazumder, Evolution of microstructure in laser deposited Al-11.28%Si alloy, Surf. Coatings Technol. 206 (2012) 2152–2160. https://doi.org/10.1016/j.surfcoat.2011.09.051.

[60] S. Kou, Welding Metallurgy, Second edi, John Wiley & Sons, Hoboken, NJ, USA, 2002. https://doi.org/10.1002/0471434027.

[61] V. Ocelík, I. Furár, J.T.M. De Hosson, Microstructure and properties of laser clad coatings studied by orientation imaging microscopy, Acta Mater. 58 (2010) 6763–6772. https://doi.org/10.1016/j.actamat.2010.09.002.

[62] H.L. Wei, J. Mazumder, T. DebRoy, Evolution of solidification texture during additive manufacturing, Sci. Rep. 5 (2015) 1–7. https://doi.org/10.1038/srep16446.

[63] S.N. Samaras, G.N. Haidemenopoulos, Modelling of microsegregation and homogenization of 6061 extrudable Al-alloy, J. Mater. Process. Technol. 194 (2007) 63–73. https://doi.org/10.1016/j.jmatprotec.2007.03.126.

[64] Y. Birol, Precipitation during homogenization cooling in AlMgSi alloys, Trans. Nonferrous Met. Soc. China (English Ed. 23 (2013) 1875–1881. https://doi.org/10.1016/S1003-6326(13)62672-2.

[65] Y. Shen, Comportement et endommagement des alliages d ' aluminium 6061-T6 : approche micromécanique To cite this version : HAL Id : pastel-00820764 École doctorale n ° 432 : Sciences des Métiers de l ' Ingénieur l ' École nationale supérieure des mines de Paris Sp, (2013).

[66] N.C.W. Kuijpers, F.J. Vermolen, K. Vuik, S. Van Der Zwaag, A model of the β-AlFeSi to α-Al(FeMn)Si transformation in Al-Mg-Si alloys, Mater. Trans. 44 (2003) 1448–1456. https://doi.org/10.2320/matertrans.44.1448.

[67] N. Kuijpers, Kinetics of the β-AlFeSi to α-Al (FeMn) Si transformation in Al-Mg-Si alloys, 2004.

[68] N.C.W. Kuijpers, W.H. Kool, P.T.G. Koenis, K.E. Nilsen, I. Todd, S. Van der Zwaag, Assessment of different techniques for quantification of α-Al(FeMn)Si and β-AlFeSi intermetallics in AA 6xxx alloys, Mater. Charact. 49 (2002) 409–420. https://doi.org/10.1016/S1044-5803(03)00036-6.

[69] C. Flament, Etude des évolutions microstructurales sous irradiation de l'alliage d'aluminium 6061-T6, Thèse de doctorat, Université de Grenoble Alpes, 2016.

[70] O.R. Myhr, Grong, H.G. Fjær, C.D. Marioara, Modelling of the microstructure and strength evolution in al-mg-si alloys during multistage thermal processing, Acta Mater. 52 (2004) 4997–5008. https://doi.org/10.1016/j.actamat.2004.07.002.

[71] C.D. Marioara, J. Nakamura, K. Matsuda, S.J. Andersen, R. Holmestad, T. Sato, T. Kawabata, S. Ikeno, HAADF-STEM study of β-type precipitates in an over-aged Al-Mg-Si-Ag alloy, Philos. Mag. 92 (2012) 1149–1158. https://doi.org/10.1080/14786435.2011.642319.

[72] R. Vissers, M.A. van Huis, J. Jansen, H.W. Zandbergen, C.D. Marioara, S.J. Andersen, The crystal structure of the β′ phase in Al-Mg-Si alloys, Acta Mater. 55 (2007) 3815–3823. https://doi.org/10.1016/j.actamat.2007.02.032.

[73] D. Maisonnette, Influences mécaniques et métallurgiques de procédés haute température sur un alliage d ' aluminium 6061-T6 par, (2010).

[74] M.W. Zandbergen, Q. Xu, A. Cerezo, G.D.W. Smith, Study of precipitation in Al-Mg-Si alloys by Atom Probe Tomography I. Microstructural changes as a function of ageing temperature, Acta Mater. 101 (2015) 136–148. https://doi.org/10.1016/j.actamat.2015.08.017.

[75] H.W. Zandbergen, S.J. Andersen, J. Jansen, Structure determination of Mg5Si6:particles in Al by dynamic electron diffraction studies, 1997. https://doi.org/10.1126/science.277.5330.1221.

[76] H.K. Hasting, W. Lefebvre, C. Marioara, J.C. Walmsley, S. Andersen, R. Holmestad, F. Danoix, Comparative study of the β″-phase in a 6xxx Al alloy by 3DAP and HRTEM, Surf. Interface Anal. 39 (2007) 189–194. https://doi.org/10.1002/sia.2487.

[77] M. Kenyon, J. Robson, J. Fellowes, Z. Liang, Effect of Dispersoids on the Microstructure Evolution in Al–Mg–Si Alloys, Adv. Eng. Mater. 21 (2019) 1–7. https://doi.org/10.1002/adem.201800494.

[78] K. Strobel, E. Sweet, M. Easton, J.F. Nie, M. Couper, Dispersoid phases in 6xxx series aluminium alloys, Mater. Sci. Forum. 654–656 (2010) 926–929. https://doi.org/10.4028/www.scientific.net/MSF.654-656.926.

[79] L. Lodgaard, N. Ryum, Precipitation of dispersoids containing Mn and/or Cr in Al-Mg-Si alloys, Mater. Sci. Eng. A. 283 (2000) 144–152. https://doi.org/10.1016/s0921-5093(00)00734-6.

[80] M. Remøe, I. Westermann, K. Marthinsen, A methodology to assess the spatial distribution of dispersoids in Al-Mg-Si alloys, 10. (2018).

[81] M. Murayama, K. Hono, Pre-precipitate clusters and precipitation processes in Al-Mg-Si alloys, Acta Mater. 47 (1999) 1537–1548. https://doi.org/10.1016/S1359-6454(99)00033-6.

[82] O.R. Myhr, O. Grong, S.J. Andersen, Modelling of the age hardening behaviour of Al-Mg-Si alloys, Acta Mater. 49 (2001) 65–75. https://doi.org/10.1016/S1359-6454(00)00301-3.

[83] T. Saito, S. Muraishi, C.D. Marioara, S.J. Andersen, J. Røyset, R. Holmestad, The effects of low Cu additions and predeformation on the precipitation in a 6060 Al-Mg-Si alloy, Metall. Mater. Trans. A Phys. Metall. Mater. Sci. 44 (2013) 4124–4135. https://doi.org/10.1007/s11661-013-1754-3.

[84] C.D. Marioara, S.J. Andersen, J. Røyset, O. Reiso, S. Gulbrandsen-Dahl, T.E. Nicolaisen, I.E. Opheim, J.F. Helgaker, R. Holmestad, Improving thermal stability in Cu-containing Al-Mg-Si alloys by precipitate optimization, Metall. Mater. Trans. A Phys. Metall. Mater. Sci. 45 (2014) 2938–2949. https://doi.org/10.1007/s11661-014-2250-0.

[85] F. Martina, M.J. Roy, B.A. Szost, S. Terzi, P.A. Colegrove, S.W. Williams, P.J. Withers, J. Meyer, M. Hofmann, Residual stress of as-deposited and rolled wire+arc additive manufacturing Ti–6Al–4V components, Mater. Sci. Technol. (United Kingdom). 32 (2016) 1439–1448. https://doi.org/10.1080/02670836.2016.1142704.

[86] H.E. Coules, P. Colegrove, L.D. Cozzolino, S.W. Wen, Experimental measurement of biaxial thermal stress fields caused by arc welding, J. Mater. Process. Technol. 212 (2012) 962–968. https://doi.org/10.1016/j.jmatprotec.2011.12.006.

[87] B.A. Szost, S. Terzi, F. Martina, D. Boisselier, A. Prytuliak, T. Pirling, M. Hofmann, D.J. Jarvis, A comparative study of additive manufacturing techniques: Residual stress and microstructural analysis of CLAD and WAAM printed Ti-6Al-4V components, Mater. Des. 89 (2016) 559–567. https://doi.org/10.1016/j.matdes.2015.09.115.

[88] S.W. Williams, F. Martina, A.C. Addison, J. Ding, G. Pardal, P. Colegrove, Wire + Arc additive manufacturing, Mater. Sci. Technol. (United Kingdom). 32 (2016) 641–647. https://doi.org/10.1179/1743284715Y.0000000073.

[89] J.R. Hönnige, S. Williams, M.J. Roy, P. Colegrove, S. Ganguly, Residual Stress Characterization and Control in the Additive Manufacture of Large Scale Metal Structures, Residual Stress. 2016. 2 (2017) 455–460. https://doi.org/10.21741/9781945291173-77.

[90] P.A. Colegrove, H.E. Coules, J. Fairman, F. Martina, T. Kashoob, H. Mamash, L.D. Cozzolino, Microstructure and residual stress improvement in wire and arc additively manufactured parts through high-pressure rolling, J. Mater. Process. Technol. 213 (2013) 1782–1791. https://doi.org/10.1016/j.jmatprotec.2013.04.012.

[91] P.A. Colegrove, J. Donoghue, F. Martina, J. Gu, P. Prangnell, J. Hönnige, Application of bulk deformation methods for microstructural and material property improvement and residual stress and distortion control in additively manufactured components, Scr. Mater. 135 (2017) 111–118. https://doi.org/10.1016/j.scriptamat.2016.10.031.

[92] F. Martina, J. Mehnen, S.W. Williams, P. Colegrove, F. Wang, Investigation of the benefits of plasma deposition for the additive layer manufacture of Ti-6Al-4V, J. Mater. Process. Technol. 212 (2012) 1377–1386. https://doi.org/10.1016/j.jmatprotec.2012.02.002.

[93] J. Ding, P. Colegrove, J. Mehnen, S. Ganguly, P.M.S. Almeida, F. Wang, S. Williams, Thermo-mechanical analysis of Wire and Arc Additive Layer Manufacturing process on large multi-layer parts, Comput. Mater. Sci. 50 (2011) 3315–3322. https://doi.org/10.1016/j.commatsci.2011.06.023.

[94] P.A. Colegrove, F. Martina, M.J. Roy, B.A. Szost, S. Terzi, S.W. Williams, P.J. Withers, D. Jarvis, High pressure interpass rolling of Wire + Arc additively manufactured titanium components, in: Adv. Mater. Res., 2014. https://doi.org/10.4028/www.scientific.net/AMR.996.694.

[95] B.B. He, Two-Dimensional X-Ray Diffraction, 2009. https://doi.org/10.1002/9780470502648.

[96] D. Richard, M. Ferrand, G.J. Kearley, Analysis and visualisation of neutron-scattering data, J. Neutron Res. (1996). https://doi.org/10.1080/10238169608200065.

[97] V. Hauk, H. Behnken, Structural and Residual Stress Analysis by Nondestructive Methods, Transferre, Elsevier, Amsterdam, 1997. https://doi.org/10.1016/b978-0-444-82476-9.50022-0.

[98] D. Gloaguen, T. Berchi, E. Girard, R. Guillén, Measurement and prediction of residual stresses and crystallographic texture development in rolled Zircaloy-4 plates: X-ray diffraction and the self-consistent model, Acta Mater. 55 (2007) 4369–4379. https://doi.org/10.1016/j.actamat.2007.04.007.